Bulletin of Mathematical Biology (2023) 85:104
https://doi.org/10.1007/s11538-023-01210-y

Society for Mathematical Biology

ORIGINAL ARTICLE

The Dynamics of Pasture–Herbivores–Carnivores with Sigmoidal Density Dependent Harvesting

Harald Bergland[1] · Evgenii Burlakov[2,3] · John Wyller[4]

Received: 22 February 2023 / Accepted: 1 September 2023

Abstract

We investigate biomass–herbivore–carnivore (top predator) interactions in terms of a tritrophic dynamical systems model. The harvesting rates of the herbivores and the top predators are described by means of a sigmoidal function of the herbivores density and the top predator density, respectively. The main focus in this study is on the dynamics as a function of the natural mortality and the maximal harvesting rate of the top predators. We identify parameter regimes for which we have non-existence of equilibrium points as well as necessary conditions for the existence of such states of the modelling framework. The system does not possess any finite equilibrium states in the regime of high herbivore mortality. In the regime of a high consumption rate of the herbivores and low mortality rates of the top predator, an asymptotically stable finite equilibrium state exists. For this positive equilibrium to exist the mortality of the top predator should not exceed a certain threshold level. We also detect regimes producing coexistence of equilibrium states and their respective stability properties. In the regime of negligible harvesting of the top predator level, we observe a finite window of the natural top predator mortality rates for which

Harald Bergland, Evgenii Burlakov and John Wyller have contributed equally to this work.

✉ Evgenii Burlakov
eb_@bk.ru

Harald Bergland
harald.bergland@uit.no

John Wyller
john.wyller@nmbu.no

1 School of Business and Economics, Campus Harstad, University of Tromsø - The Arctic University of Norway, Havnegata 5, 9404 Harstad, Norway

2 X-Bio Institute, University of Tyumen, Volodarskogo 6, Tyumen, Russia 625003

3 Research Institute of Mathematics, Physics and Computer Sciences, Derzhavin Tambov State University, Internatsionalnaya 33, Tambov, Russia 392000

4 Department of Mathematics, Norwegian University of Life Sciences, Drøbakveien 31, 1432 Ås, Norway

Published online: 19 September 2023

oscillations in the top predator-, the herbivore- and the biomass level take place. The lower and upper bound of this window correspond to two Hopf bifurcation points. We also identify a bifurcation diagram using the top predator harvesting rate as a control variable. Using this diagram we detect several saddle node- and Hopf bifurcation points as well as regimes for which we have coexistence of interior equilibrium states, bistability and relaxation type of oscillations.

Keywords Predator–prey models · Nonlinear dynamical systems theory · Existence and stability of equilibrium states · Saddle node bifurcations · Hopf bifurcations · Relaxation oscillations

Mathematics Subject Classification 37N25 · 92D25 · 92D40

1 Introduction

The recovery of carnivores in terrestrial ecosystems causes conflicts with humans and livestock, see Kaczensky et al. (2013), Ripple et al. (2014), Boitani and Linnell (2015), Van Eeden et al. (2018) and Åhman et al. (2022) and the references therein. In Fennoscandia (Scandinavia, Finland, Kola Peninsula and Russian Karelia), such conflicts concern the depredation of livestock, especially sheep and the loss of semidomesticated reindeer (*Rangifer tarandus*).

The Sámi reindeer herders in Scandinavia and Finland share their ranges with wildlife, and livestock losses from predation are mainly attributed to lynx (*Lynx lynx*), wolverine (*Gulo gulo*) and golden eagle (*Aquila chrysaetos*). According to Tveraa et al. (2014), approximately 70 percent of the documented loss of semidomesticated reindeers in Norway is caused by lynx and wolverine. Mattisson et al. (2011) have concluded that semidomestic reindeers are the main prey for lynx in northern Scandinavian. Moreover, the return of the wolf (*Canis lupus*) causes a decimation of the reindeer population in some regions. Kojola et al. (2009) show that the annual recruitment rate of reindeer is strongly correlated with the wolf population density. Fluctuations in large carnivore and reindeer populations seem also to be well documented. See Åhman et al. (2022) and St John (2022) and the references therein. Public agencies often implement compensation programs to reduce conflicts and alleviate losses. See Tveraa et al. (2014), Bautista et al. (2019) and NEA (2022). Skonhoft et al. (2017) and Johannesen et al. (2019) study impact of predation in a reindeer population and state that predation mortality may compensate for natural mortality in situations of food scarcity, and thereby predation may improve the economic lot of livestock holders.

In western Europe, wolverines are only found in Finland, Sweden and Norway, and this is the only region containing all four large carnivore species in Europe. See Chapron et al. (2014). Wolverines became protected in Sweden in 1969, in southern Norway in 1973, and in the remaining parts of Norway in 1982. The Scandinavian wolverine population increased slowly both in Sweden and Norway during the first decades after protection (Sæther et al. 2005). Management decisions, like issuing hunting licences and harvest quotas are mainly done by public environmental agen-

cies.[1] However, according to Persson et al. (2009), poaching forms a substantial part of extraction of the wolverine population in northern Scandinavia, and causing up to 60 percent of adult mortality.

Euroasian lynx populations in Norway and Sweden are stable (Kaczensky et al. 2013), and most of the lynx populations are protected allowing a limited cull of lynx by hunters and with annual harvesting quotas depending on the regional animal population (NEA 2022; Kaczensky et al. 2013). For the study area in Scandinavia, Andrén et al. (2006) report that poaching accounts for 46 percent of the mortality in the adult lynx populations. Furthermore, both poaching and legal harvest appear to be primarily motivated by conflicts caused by lynx depredation on semidomestic reindeers in northern Scandinavia.

These observations serve as a background and motivation for the present investigation. We consider a $3D$ predator–prey model where the carnivore population and herbivore population play the roles, respectively, of predators and preys, and the herbivores feed on the vegetation. The model incorporate harvesting of herbivore and hunting for carnivores. We follow the modeling approach which is common in theoretical ecology (Murray 2002; de Roos 2014; Legović et al. 2010; Li et al. 2016), and bioeconomics (Clark 2010; Brekke et al. 2007; Johannesen and Skonhoft 2009; Johannesen 2014). Legović et al. (2010) and Ghosh et al. (2014b) apply similar models when discussing maximum sustainable yields in fisheries.[2]

Humans harvest the herbivores for the purpose of private consumption and/or commercial reasons. The two most common harvesting assumptions are a nonzero constant harvesting rate, and a piecewise linear harvesting rate (see, for example Brekke et al. 2007 and Li et al. 2016 and the references therein). In Bergland et al. (2019) a $2D$ predator–prey model for the biomass—herbivore interaction is investigated. In that model the harvesting rate is given as a sigmoidal function in the herbivore population density.

In our tritrophic model we assume that the harvesting effects for both the herbivores and the carnivores are described by means of sigmoidal functions of the same type as used in Bergland et al. (2019). The arguments for this assumption proceed as follows:

For small and moderate population levels we assume that the harvesting rates to grow approximately linearly with the population level. Moreover, we have a slow growth of the harvesting rate functions for small population levels. A saturation of the harvesting rates sets in for larger population levels. Finally, but not least we have a smooth transition between the low and high level of the population densities. The saturation property indeed signifies a limitation in the human intervention capacity when it comes to harvesting. We believe that the sigmoidal representation of the harvesting rates mimics a more realistic scenario as compared with the constant non-

[1] For more details on management institutions and legislation see Kaczensky et al. (2013), Åhman et al. (2022) and NEA (2022).

[2] This kind of modeling has also examined interactions between different marine tropical levels (e.g.krill/fish/whales) and the consequences for fishery management. See May et al. (1979), Beddington and May (1980), Flaaten (1988), Hogarth et al. (1992), Flaaten (1991), Brown et al. (2005), Ghosh and Kar (2013), Huang et al. (2013), Ghosh et al. (2014a), Paul et al. (2016), Tromeur and Loeuille (2017), Barman and Ghosh (2019). Models of the Lotka–Volterra type are also applied in other settings, e.g. Vázquez and Watt (2011).

zero harvesting rate assumption, the proportional harvesting term or a harvesting rate decomposing in proportional harvesting term for small and moderate population regime connected to non-zero constant level when the population level exceeds a certain threshold. By using this modelling approach we are able to study how the harvesting practice at two tropical levels influence the coexistence of carnivore and herbivore populations. The model analyses expose how the natural mortality rate of the top predators in combination with the harvesting rate of the top predator is crucial for the existence of equilibrium states and the stability of these states.

The present paper is organized as follows: In Sect. 2 we present our modeling framework, while Sect. 3 deals with the general mathematical properties of the model (scaling, wellposedness, positive persistence, global boundedness of the solutions, and existence and stability of equilibrium states). In Sect. 4 we detail numerically the evolution of the population levels with particular emphasis on the role of the equilibrium states. The Sects. 5–7 deal with the existence of different bifurcation phenomena (Hopf- and saddle node bifurcations), bistability and the excitation of the relaxation type of oscillations in the present modelling framework. Section 8 contains concluding remarks (Sect. 8.1) and an outlook (Sect. 8.2). In the appendices A–D we detail the mathematical properties of our modelling framework.

2 Model

We consider a 3D predator–prey model in which the food resources (preys) dynamics is coupled to the change of the herbivore population density. The herbivores act as food resources for the top predators. We also account for harvesting of both the herbivore population and the top predators. Let z, y and x denote the top predator population density, the herbivore population density and the biomass density. The actual predator–prey model reads

$$\left.\begin{aligned}
\frac{dz}{dt} &= \overbrace{rcyz}^{\text{growth}} - \overbrace{lz}^{\text{death}} - \overbrace{H(z; z_0, L_{\max}, k)}^{\text{harvesting}},\\
\frac{dy}{dt} &= \overbrace{qbxy}^{\text{growth}} - \overbrace{cyz}^{\text{consumption}} - \overbrace{my}^{\text{death}} - \overbrace{H(y; y_0, H_{\max}, p)}^{\text{harvesting}},\\
\frac{dx}{dt} &= \overbrace{\sigma x(1-\frac{x}{K})}^{\text{growth}} - \overbrace{bxy}^{\text{consumption}},
\end{aligned}\right\} \tag{1}$$

where we have specified the role of each term in this model. The biological interpretation of the variables and parameters in (1) is summarized in Table 1.

The first term on the right hand side of the third equation in (1) models the food resources for the herbivores, adjusted with the logistic growth which describes the natural saturation of the biomass growth due to some kind of resource limitation. The second term measures the reduction in the biomass caused by the herbivores. The second equation in (1) is the herbivore predator equation, where the first term on the

Table 1 The fundamental units are T for time (e.g., $year, month$) and M for mass (e.g., $tons, kg$)

Variables/parameters	Biological interpretation	Measurement units
t	Time	T
z	Top predator population density	M
y	Herbivore population density (predators)	M
x	Biomass density (preys)	M
K	Carrying capacity of the prey biomass	M
σ	Intrinsic growth rate for the biomass density	T^{-1}
b	Consumption rate per herbivore animal	$M^{-1}T^{-1}$
q	Conversion efficiency coefficient for the herbivores (with $0 < q < 1$)	$Dimensionless$
m	Intrinsic mortality rate of the herbivores	T^{-1}
c	Consumption rate per predator animal	$M^{-1}T^{-1}$
r	Conversion efficiency coefficient for the top predators (with $0 < r < 1$)	$Dimensionless$
l	Intrinsic mortality rate of the top predators	T^{-1}
Φ	Relative harvesting rate per animal	MT^{-1}
$H_{\max}$	Saturated harvesting rate of the herbivores	MT^{-1}
y_0	Herbivore density for which the harvesting rate is $\frac{1}{2}H_0$	M
p	Steepness parameter of the herbivore harvesting rate function (with $p > 1$)	$Dimensionless$
$L_{\max}$	Saturated harvesting rate of the top predators	MT^{-1}
z_0	Top predator density for which the harvesting rate is $\frac{1}{2}L_0$	M
k	Steepness parameter of the top predator harvesting rate function (with $k > 1$)	$Dimensionless$

right hand side models the increase of the herbivore density per unit time. The second term on the right hand side in this equation accounts for the depletion of herbivores per unit time due to the fact that these animals act as food resources for the top predators. The third term accounts for the natural mortality of the herbivores, whereas the last term models the effect of harvesting by humans. Finally, the first equation is the top predator equation. The first term on the right hand side of this equation represents the increase per unit time of the top predators caused by the access of the food resources. The second term takes care of the natural mortality of the top predators and the third term accounts for harvesting of the top predators caused by humans. We specify the harvesting rate H in the following way: It constitutes a 3-parameter family of functions given as

$$\left.\begin{aligned} H(u; u_0, \tilde{H}_{\max}, g) &= \tilde{H}_{\max} u \Phi(u; u_0, g), \\ \Phi(u; u_0, g) &= \frac{u^{g-1}}{u^g + u_0^g}, \end{aligned}\right\} \tag{2}$$

where $u, \tilde{H}_{\max} \geq 0, u_0 > 0, g > 1$. The parameter g is referred to as the steepness parameter, whereas the parameter $\tilde{H}_{\max}$ plays the role as the saturation level of the harvesting rate, i.e.,

$$\lim_{u\to\infty} H(u; u_0, \tilde{H}_{\max}, g) = \tilde{H}_{\max}^{(-)}.$$

The parameter u_0 which has the same dimension as u is a typical predator density defined in the following way: It yields a harvesting rate which is half the saturation level $H_{\max}$ i.e.

$$H(u_0; u_0, \tilde{H}_{\max}, g) = \frac{1}{2}\tilde{H}_{\max}.$$

We refer to u_0 as the characteristic density. The parameter g measures the steepness of the harvesting rate for $u \sim u_0$ i.e.

$$H'(u; u_0, \tilde{H}_{\max}, g) \sim g \quad \text{when } u \sim u_0. \tag{3}$$

The function Φ has a unique maximum point u_m with corresponding maximal value $\Phi(u_m)$ given as

$$u_m = (g-1)^{1/g} u_0, \quad \Phi(u_m) = \frac{1}{u_0} \cdot \varphi(g), \quad \varphi(g) \equiv \frac{(g-1)^{1-1/g}}{g}. \tag{4}$$

Notice that the analytical structure of the harvesting rate functions is the same for the carnivores and the herbivores. The replacement $(u; u_0, \tilde{H}_{\max}, g) = (z; z_0, L_{\max}, k)$ in (2) yields the harvesting rate function for the top predators, whereas the replacement $(u; u_0, \tilde{H}_{\max}, g) = (y; y_0, H_{\max}, p)$ in (2) produces the harvesting rate function for the herbivores. The graph of the harvesting rate H is sketched in Fig. 1a for two different values of the characteristic density u_0 and the steepness parameter g. Greater emphasis on carnivore protection is interpreted in this model as lowering the harvesting saturation level of the top predators. Furthermore, we notice that a high value of the steepness parameter k could be interpreted as a hunting practice where the animals are more strictly protected if the population is below a certain threshold, but are subject to a relatively extensive harvesting for $z \sim z_0$, see expression (3). This threshold or characteristic density could be interpreted as a public population target for the top predator species described in NEA (2022). In the forthcoming numerical studies we have accounted for this by letting $k = 8$, $z_0 = 0.2$ and $p = 4$, $y_0 = 0.4$. In Fig. 1 we show the graph of the harvesting rate function in these two cases. The blue coloured graph in this figure signifies the harvesting rate for the top predators, whereas the red coloured graph shows the harvesting rate for the herbivores. Furthermore, we will examine impacts of varying the harvesting saturation level $L_{\max}$ of the top predators on the dynamical output from the model. To complete this we also show the graph of the scaling function Φ for different values of the steepness parameter g and the characteristic density u_0 in Fig. 1b.

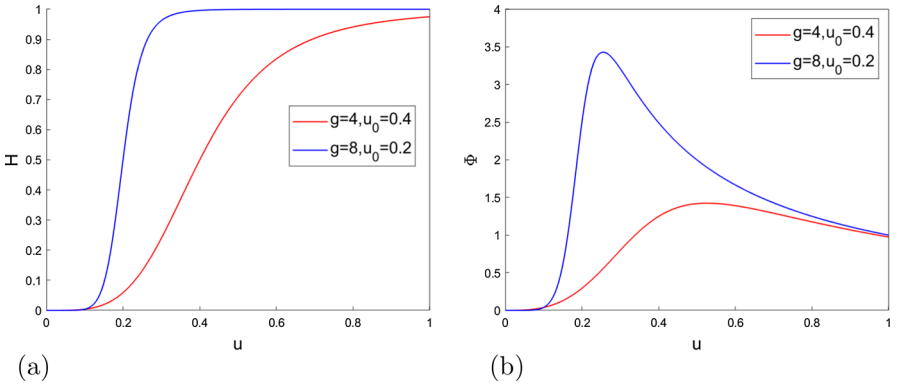

Fig. 1 **a** The graph of the harvesting rate function H defined by (2) for $\tilde{H}_{\max} = 1$. **b** The graph of the scaling function Φ defined by means of (2). Input parameters are given in Table 3

3 General Properties of the Model: Existence and Stability of Equilibrium Points

In the Sects. 3.1–3.4 we explore in depth the properties of the model (1). We carry out the analysis by making use of standard methods for dynamical systems as presented in (Guckenheimer and Holmes 1983; Logan 1987) and numerical simulations.

3.1 Scaling and General Properties of the Model

We start by scaling the system (1) (Logan 1987) by introducing the non-dimensional variables and parameters θ, η, ξ, τ, β, μ, ν, η_0, γ and θ_0 defined by

$$\left.\begin{aligned} &x(t) = K\xi(\tau), \quad y(t) = K\eta(\tau), \quad z(t) = K\theta(\tau), \quad \tau = \sigma t, \\ &\beta = \frac{bK}{\sigma}, \quad \nu = \frac{H_{\max}}{qbK^2}, \quad \mu = \frac{m}{qbK}, \quad y_0 = K\eta_0, \\ &\zeta = \frac{cK}{\sigma}, \quad \varrho = \frac{c}{qb}, \quad \gamma = \frac{l}{rcK}, \quad \epsilon = \frac{L_{\max}}{rcK^2}, \quad z_0 = K\theta_0. \end{aligned}\right\} \tag{5}$$

We then get

$$\left.\begin{aligned} \frac{d\theta}{d\tau} &= r\zeta\theta\mathcal{H}(\theta, \eta, \xi; \gamma, \epsilon, \theta_0, k), \\ \frac{d\eta}{d\tau} &= q\beta\eta\mathcal{G}(\theta, \eta, \xi; \varrho, \mu, \nu, \eta_0, p), \\ \frac{d\xi}{d\tau} &= \xi\mathcal{F}(\theta, \eta, \xi; \beta), \end{aligned}\right\} \tag{6}$$

Table 2 The normalized predator–prey model (6)–(7)

Non-dimensional variables/parameters	Biological interpretation
$\tau = \sigma t$	Dimensionless time
$\xi = \frac{x}{K}$	Normalized biomass density (preys)
$\eta = \frac{y}{K}$	Normalized herbivore predator biomass
$\theta = \frac{z}{K}$	Normalized top predator biomass
$\beta = \frac{bK}{\sigma}$	Normalized consumption rate per herbivore animal
$\mu = \frac{m}{qbK}$	Normalized mortality rate of the herbivores
$\nu = \frac{H_{\max}}{qbK^2}$	Normalized saturation level of the harvesting rate of herbivores
$\eta_0 = \frac{y_0}{K}$	Normalized typical herbivore density
p	Steepness parameter of the herbivore harvesting rate function (with $p > 1$)
q	Conversion efficiency coefficient for the herbivores (with $0 < q < 1$)
$\zeta = \frac{cK}{\sigma}$	Normalized consumption rate per top predator animal
$\gamma = \frac{l}{rcK}$	Normalized mortality rate of top predators
$\epsilon = \frac{L_{\max}}{rcK^2}$	Normalized saturation level of the harvesting rate of top predators
$\theta_0 = \frac{z_0}{K}$	Normalized typical top predator density
k	Steepness parameter of the top predator harvesting rate function (with $k > 1$)
r	Conversion efficiency coefficient for the top predators (with $0 < r < 1$)
$\varrho = \frac{c}{qb}$	Consumption rate of top predators versus the effective consumption rate of the herbivores

from (1) where the functions $\mathcal{H}$, $\mathcal{G}$ and $\mathcal{F}$ are defined as

$$\left.\begin{aligned} &\mathcal{H}(\theta, \eta, \xi; \gamma, \epsilon, \theta_0, k) \equiv \eta - \gamma - \epsilon\Phi(\theta; \theta_0, k), \\ &\mathcal{G}(\theta, \xi, \eta; \varrho, \mu, \nu, \eta_0, p) \equiv \xi - \varrho\theta - \mu - \nu\Phi(\eta; \eta_0, p), \\ &\mathcal{F}(\theta, \eta, \xi; \beta) \equiv 1 - \xi - \beta\eta. \end{aligned}\right\} \tag{7}$$

The interpretation of the non-dimensional quantities in the system (6)–(7) is summarized in Table 2. We notice that the non-dimensional parameters β, μ, ϱ, ν and η_0 are direct proportional to the consumption rate per herbivore animal (b), the intrinsic mortality rate of the herbivores (m), the consumption rate per top predator animal (c), the saturation level of the harvesting rate ($H_{\max}$) and the typical herbivore density y_0, respectively. The parameters γ, ϵ and θ_0 in the top predator equation are as follows: γ and ϵ measure the strengths of the mortality rate l and the saturated harvesting rate $L_{\max}$ of the top predators. θ_0 represents the typical top predator density. We also notice that ϱ can be expressed as the ratio $q^{-1} \cdot \frac{\zeta}{\beta}$ where $\zeta = \frac{cK}{\sigma}$ and $\beta = \frac{bK}{\sigma}$ model the nor-

malized consumption rate per top predator animal and herbivore animal, respectively. Finally, we have normalized the time t against the intrinsic logistic timescale σ^{-1} of the biomass, the biomass density x, the herbivore density y and the top predator density z against the carrying capacity K of the biomass to get the non-dimensional variables τ, ξ, η and θ.

Notice the following structural similarity of non-dimensional quantities in the system (6)–(7):

- The normalized mortality rate μ $(= \frac{m}{qbK})$ of the herbivores and the normalized mortality rate γ $(= \frac{l}{rcK})$ of the top predators.
- The normalized saturation level of the harvesting rate ν $(= \frac{H_{\max}}{qbK^2})$ of the herbivores and the normalized saturation level of the harvesting rate ϵ $(= \frac{L_{\max}}{rcK^2})$ of the top predators.
- The effective normalized consumption rate per herbivore animal $q\beta$ $(= \frac{qbK}{\sigma})$ in the herbivore equation and the effective normalized consumption rate per top predator animal $r\zeta$ $(= \frac{rcK}{\sigma})$ in the top predator equation.

We expect that the magnitude of the ratio $L_{\max}/H_{\max}$ is important when dealing with management and harvesting regulation. By making use of Table 2 we observe that this ratio can be expressed as

$$\frac{L_{\max}}{H_{\max}} = \frac{\epsilon}{\nu} r\varrho = \frac{\epsilon}{\nu} \cdot \frac{rc}{qb}, \tag{8}$$

which shows that this ratio is directly proportional to the ratio ϵ/ν. The proportionality constant rc/qb is interpreted as the effective consumption rate per top predator animal divided by the effective consumption rate per herbivore animal. Thus, the study of the regime $L_{\max} \ll H_{\max}$ translates into the regime $\epsilon \ll \nu$. It is less likely that one can control the ratio rc/qb through human intervention, while the ratio ϵ/ν is interpreted as a regulatory tool in our modelling framework. The upcoming analysis will also show the significance of both the natural mortality (γ) and the harvesting mortality (ϵ) of the top predators. We will refer to the parameters γ and ϵ as *the decimation parameters of the top predators*.

To summarize, due to the definition of the parameters listed in Table 2, we conveniently divide them into the following three groups:

- Group 1 which consists of q, β, μ, ν, η_0 and p is termed the *herbivore parameter set*.
- Group 2 which consists of r, ζ, γ, ϵ, θ_0 and k is termed the *top predator parameter set*.
- Group 3 consists of the parameter ϱ. The normalized consumption rate per top predator is directly proportional to ϱ, i.e.,

$$\zeta = q\beta\varrho, \tag{9}$$

with the effective consumption rate per herbivore $q\beta$ as a proportionality constant. This means that ϱ represents the degree of coupling between the herbivore popu-

lation level and the top predator level. We therefore refer to this parameter as the *herbivore-top predator coupling parameter*.

In Appendix D we prove that the solution of the initial value problem of the system (6)–(7) exists, is unique and is bounded for all $\tau \geq 0$ (Theorem 3). Secondly, by proceeding in a way analogous to Appendix A in Bergland et al. (2019), we conclude that the system (6)–(7) satisfies the *the positive invariance property* or *the positive persistence property*. This means that any orbit of the system (6)–(7) starting in the first orthant of the θ, η, ξ-space remains in that part of the phase space (and will not cross the coordinate planes in $\mathbb{R}^3$). Thus the model under consideration possesses the biologically sensible property that the biomass density, the herbivore population density and the top predator population density will remain positive and bounded for all $t > 0$.

In the forthcoming numerical simulations we will make use of the input parameters listed in Set A, Set B and Set C in Table 3. These parameter values have been chosen with the intention of highlighting the rich dynamical properties of the model, and as confirmation of the general results. From the forthcoming analyse it follows that these sets produce different numbers of equilibrium states and different dynamical features.

Remark 1 We observe the following notable features for the input parameters sets listed in Table 3:

- For Set A we will show that we have coexistence of three equilibrium points characterized by no top predators and three finite equilibrium points, see Table 5.
- Set B is characterized by an increased natural mortality rate of the top predators as compared with Set A: The normalized mortality rate γ of the top predator (Group 1 parameter) is increased from $\gamma = 0.15$ in set A to $\gamma = 0.45$ in set B. The outcome here is three boundary equilibrium points characterized by no top predators and two finite equilibrium points, see Table 5.
- Set C describes a scenario with more vigorous and healthy herbivores and at the same time lower taxation of top predators, as compared to the situation modelled by means of Set A. Set C appears by changing four of the parameters in Set A: The normalized consumption rate β of the herbivores is increased from $\beta = 0.1$ to $\beta = 0.15$, and the normalized mortality rate μ of the herbivores is reduced from $\mu = 0.45$ to $\mu = 0.25$. In addition, the consumption rate of top predators versus the effective consumption rate of the herbivores (the coupling parameter ϱ) is increased from $\varrho = 0.2$ to $\varrho = 0.6$. This increase may be caused by an increase in the consumption rate per top predator animal c as compared with the situation described by means of Set A. Finally, the normalized saturation level of the top predator harvesting rate function, i.e., the Group 2 parameter ϵ is reduced from $\epsilon = 0.5$ to $\epsilon = 0.2$. Here we will show that we get only one boundary equilibrium point characterized by no top predators and three finite equilibrium points, see Table 5. Notice also that the chosen changes in β and ϱ also imply that the normalized consumption rate per top predator animal ζ increases from 0.014 in Set A to 0.063 in set C.

Finally, we compute the ratio $L_{\max}/H_{\max}$ given by the formula (8) for the three input parameter sets in Table 3: $L_{\max}/H_{\max} = 0.225$ (Set A and Set B), $L_{\max}/H_{\max} = 0.27$ (Set C).

Table 3 Input parameters for forthcoming numerical simulations in the present paper

Parameters	q	β	μ	ν	η_0	p	$\mathcal{Q}_m$	r	ζ	γ	ϵ	θ_0	k	$\eta_{\max}$	ϱ
Set A	0.7	0.1	0.55	0.4	0.4	4	1.12	0.9	0.014	0.15	0.5	0.2	8	1.87	0.2
Set B	0.7	0.1	0.55	0.4	0.4	4	1.12	0.9	0.014	0.45	0.5	0.2	8	2.17	0.2
Set C	0.7	0.15	0.25	0.4	0.4	4	0.82	0.9	0.063	0.15	0.2	0.2	8	0.84	0.6

Here ζ, $\mathcal{Q}_m$ and $\eta_{\max}$ are computed by means of (9), (17) and (26), respectively

3.2 Dynamics in the Boundary of the First Orthant

Considering the motion in the positive coordinate planes, i.e., when $\theta = 0$, $\eta = 0$ and $\xi = 0$, we notice that the model (6)–(7) restricted to each of these coordinate planes possesses the positive invariance property in each of these planes.

Now we assume $\theta = 0$. As expected our model in this case simplifies to the herbivore—biomass model investigated in Bergland et al. (2019).

Then we consider the case $\eta = 0$. In that case the dynamical evolution is governed by means of subsystem of decoupled ordinary differential equations

$$\left.\begin{aligned} \frac{d\theta}{d\tau} &= -r\zeta\theta(\gamma + \epsilon\Phi(\theta;\theta_0,k)),\\ \frac{d\xi}{d\tau} &= \xi(1-\xi). \end{aligned}\right\} \tag{10}$$

Now, since

$$0 \le \Phi(\theta;\theta_0,k) \le \Phi(\theta_m;\theta_0,k)\ \left(= \frac{(k-1)^{1-1/k}}{k\theta_0}\right),$$

for all $\theta \ge 0$, we find the bounding inequality

$$-r\zeta\theta\big[\gamma + \epsilon\Phi(\theta_m;\theta_0,k)\big] \le \frac{d\theta}{d\tau} \le -r\zeta\gamma\theta,$$

for the derivative $\frac{d\theta}{d\tau}$ from (10). Hence it follows that the solution of the θ-equation is bounded by exponentially decaying functions from both above and below, i.e.,

$$\theta(0)\exp\big[-r\zeta\big(\gamma + \epsilon\Phi(\theta_m;\theta_0,p)\big)\tau\big] \le \theta(\tau) \le \theta(0)\exp\big[-r\zeta\gamma\tau\big],$$

in this case. Here $\theta_m \equiv z_m/K$ denotes the maximum point of the function $\Phi(\cdot;\theta_0,k)$, see (4). We also observe that $r\zeta\gamma = l/\sigma$. By restoring to the dimensional setting we therefore find that the top predator mortality time scale $1/l$ is the typical time scale for the decay of the top predator population. We conclude that $\theta(\tau) \to 0^+$ as $\tau \to +\infty$. This indicates that with no herbivore population present, the top predator population will finally go extinct. The biomass will evolve according to the standard logistic equation, and hence the biomass will stabilize on the carrying capacity K.

Then we investigate the scenario with negligible biomass, i.e., with $\xi \approx 0$. In that case our governing system is approximated with the simplified $2D$-system

$$\left.\begin{aligned} \frac{d\Omega}{ds} &= r\varrho\Omega(\Lambda - \gamma - \epsilon\Phi(\Omega;\theta_0,k)),\\ \frac{d\Lambda}{ds} &= -\Lambda(\varrho\Omega + \mu + \nu\Phi(\Lambda;\eta_0,p)) \end{aligned}\right\}, \tag{11}$$

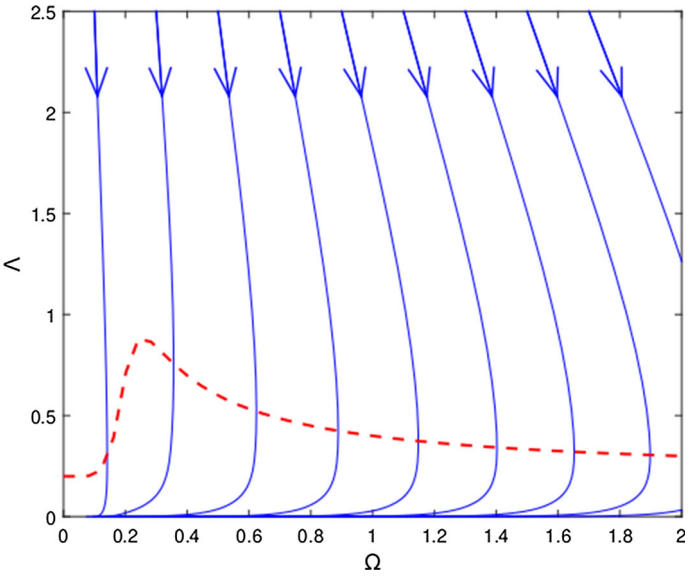

Fig. 2 The phase portrait of the non-biomass system (11). Blue curves are the orbits of this system. The red dashed curve is the graph of the nullcline (13). The input parameters are given by Set *A* in Table 3 (Color figure online)

by making use of the rescaling

$$s = q\beta\tau, \quad \theta(\tau) = \Omega(s), \quad \eta(\tau) = \Lambda(s), \tag{12}$$

and the fact that $r\varrho = \frac{r\zeta}{q\beta}$. From the second equation we notice that Λ is a monotonically decreasing function of s. The behavior of the dynamical system can thus be summarized by means of the phase portrait of the autonomous dynamical system. The nullcline

$$\Lambda = \gamma + \epsilon\Phi(\Omega; \theta_0, k), \tag{13}$$

of this system plays an essential role in the behavior of this system: Let $\mathcal{A}$ denote the subset

$$\mathcal{A} = \{(\Omega, \Lambda) \in \mathbb{R}^2_+; \quad \Lambda > \gamma + \epsilon\Phi(\Omega; \theta_0, k)\},$$

of the first quadrant in the Ω, Λ-plane. If we choose the initial value condition $(\Omega(0), \Lambda(0))$ such that $(\Omega(0), \Lambda(0)) \in \mathcal{A}$, the dynamical system (11) predicts an increase in top predator level and a decrease in the the herbivore population in the initial phase of the temporal evolution. The top predator population attains its maximum in finite time corresponding to a vertical crossing of the orbits with the nullcline (13) before a decline in the top predator population sets in. In the final stage of the evolution (i.e., when $\tau \to +\infty$) we find that both θ and η approach zero. The phase plane analysis of the system (11) is summarized in Fig. 2.

3.3 Equilibrium Points of the Model

3.3.1 Boundary Equilibrium Points

On the boundary of the positive orthant in the θ, η, ξ-space the points $P_0 = (0, 0, 0)$ and $P_1 = (0, 0, 1)$ are equilibrium states. In addition, we have at least one equilibrium point of the type $P^* = (0, \eta^*, \xi^*)$ provided $0 \leq \mu \leq 1$ where the coordinates η^* and ξ^* are determined by the procedure outlined in Bergland et al. (2019). For the sake of completeness we recall this procedure here: $\eta = \eta^*$ is a zero of the function Δ defined by

$$\Delta(\eta; \beta, \mu, \nu, \eta_0, p) \equiv \mathcal{P}(\eta; \beta) - \mathcal{Q}(\eta; \mu, \nu, \eta_0, p), \tag{14}$$

where

$$\mathcal{P}(\eta; \beta) \equiv 1 - \beta\eta, \tag{15}$$

$$\mathcal{Q}(\eta; \mu, \nu, \eta_0, p) \equiv \mu + \nu\Phi(\eta; \eta_0, p). \tag{16}$$

Note that the function Δ has no zeros if $\mu > 1$, whereas Δ has at least one zero in the interval $(0, 1/\beta)$ when $0 \leq \mu \leq 1$. The maximal number of zeros of Δ in this interval is three. The equilibrium point P^* merges together with P_1 when $\mu \to 1^-$. We summarize the existence theory for the equilibrium states $P^* = (0, \eta^*, \xi^*)$ in Table 4. Here

$$\mathcal{Q}_m \equiv \mathcal{Q}(\eta_m; \mu, \nu, \eta_0, p) = \mu + \frac{\nu}{\eta_0} \cdot \varphi(p), \quad \varphi(p) \equiv \frac{(p-1)^{1-1/p}}{p}, \tag{17}$$

where $\eta_m \equiv (p-1)^{1/p}\eta_0$ is the maximum point of $\mathcal{Q}$, see (4). We have detailed the properties of the function Δ in Appendix A. Table 4 outlines the main results of this investigation. When selecting the herbivore parameters β, μ, ν, η_0 and p as in Table 3 we readily find that

$$\eta_1^* = 0.3462, \quad \eta_2^* = 1.1955, \quad \eta_3^* = 3.2812, \quad 1/\beta = 10 \quad \text{(Sets } A, B\text{)}, \tag{18}$$

$$\eta^* = 4.3930, \quad 1/\beta = 6.67 \quad \text{(Set } C\text{)}, \tag{19}$$

by using the procedure detailed in Appendix A[3]

3.3.2 Positive Equilibrium Points

We investigate the possibility of having equilibrium points in the interior of the first orthant in the θ, η, ξ-space, i.e., points $P_e = (\theta_e, \eta_e, \xi_e)$ for which $\theta_e, \eta_e, \xi_e > 0$. We

[3] Note that (η^*, ξ^*) denote the interior equilibrium points of the first quadrant as detected in Bergland et al. (2019).

Table 4 The number of boundary equilibrium points $P^* = (0, \eta^*, \xi^*)$ as a function of the normalized consumption rate β in the regime $0 \leq \mu < 1$ for the normalized mortality rate of the herbivores

Maximal value of $\mathcal{Q}$	Range of β	Number of boundary equilibrium points P^*
$\mathcal{Q}_m > 1$	$\beta > \beta_{cr}$	1
	$\beta = \beta_{cr}$	2
	$0 < \beta < \beta_{cr}$	3
$\mathcal{Q}_m \leq 1$	$\beta > \beta_{cr,2}$	1
	$\beta = \beta_{cr,2}$	2
	$\beta_{cr,1} < \beta < \beta_{cr,2}$	3
	$\beta = \beta_{cr,1}$	2
	$0 < \beta < \beta_{cr,1}$	1

See Appendix 1 for details

refer to such equilibrium points as *positive equilibrium points*. If positive equilibrium points P_e exist, they must satisfy the system of equations

$$\mathcal{H}(\theta_e, \eta_e, \xi_e; \gamma, \epsilon, \theta_0, k) = 0, \tag{20}$$

$$\mathcal{G}(\theta_e, \eta_e, \xi_e; \varrho, \mu, \nu, \eta_0, p) = 0, \tag{21}$$

$$\mathcal{F}(\theta_e, \eta_e, \xi_e; \beta) = 0. \tag{22}$$

We readily find that this system is equivalent with the set of equations

$$\theta_e = V(\eta_e) \equiv \frac{1}{\varrho}\Delta(\eta_e; \beta, \mu, \nu, \eta_0, p) = \frac{1}{\varrho}\big[1 - \beta\eta_e - \mu - \nu\Phi(\eta_e; \eta_0, p)\big], \tag{23}$$

$$\eta_e = U(\theta_e) \equiv \mathcal{Q}(\theta_e; \gamma, \epsilon, \theta_0, k) \equiv \gamma + \epsilon\Phi(\theta_e; \theta_0, k), \tag{24}$$

$$\xi_e = \mathcal{P}(\eta_e; \beta) \equiv 1 - \beta\eta_e. \tag{25}$$

Here the function Δ is defined by means of (14). The function U has a global maximum point $\theta_e = \theta_m = (k-1)^{1/k}\theta_0$ and a global minimum point at $\theta_e = 0$. Hence U satisfies the bounding inequality

$$\gamma \leq U(\theta_e) \leq \eta_{\max} \quad \text{for all } \theta_e \geq 0,$$

where

$$\eta_{\max} \equiv U(\theta_m) = \gamma + \epsilon\Phi(\theta_m; \theta_0, k) = \gamma + \frac{\epsilon}{\theta_0} \cdot \varphi(k), \quad \varphi(k) \equiv \frac{(k-1)^{1-1/k}}{k}, \tag{26}$$

which by appealing to (24) means that a necessary condition for the existence of a positive equilibrium point P_e is that the η_e-coordinate of P_e satisfies the localization requirement

$$\gamma \leq \eta_e \leq \eta_{\max}. \tag{27}$$

Mark the role of the parameter $\eta_{\max}$: This parameter is a linear function of ϵ, i.e., the normalized saturation level of the harvesting rate of top predators ϵ. This means that this parameter takes care of the impact of both the mortality (γ) and harvesting of the top predators (ϵ).

According to (26), the width of the interval $\mathcal{V}_U$ defined by

$$\mathcal{V}_U \equiv [\gamma, \eta_{\max}], \tag{28}$$

can be expressed in terms of the top predator maximal and normalized harvesting ratio ϵ/θ_0 and the steepness parameter k of the top predator harvesting rate function, i.e.,

$$m(\mathcal{V}_U) \equiv \eta_{\max} - \gamma = \frac{\epsilon}{\theta_0} \cdot \varphi(k). \tag{29}$$

Interestingly, we find that $\varphi(k) \to 1^-$ when $k \to 1^+$ and $k \to +\infty$, whereas φ possesses a global minimum point at $k = 2$ with a corresponding global minimum value given as $\varphi(2) = 1/2$, from which it follows that the width of the interval $\mathcal{V}_U$ obeys the bounding inequality

$$\frac{1}{2} \cdot \frac{\epsilon}{\theta_0} \leq m(\mathcal{V}_U) \leq \frac{\epsilon}{\theta_0}, \tag{30}$$

for all $k > 1$. Thus we conclude that *the maximal value of the scaling function* Φ *of the top predator harvesting rate determines the width of the interval* $\mathcal{V}_U$. This means that the impact of the top predators on the positive equilibrium problem is taken care of by means of this interval.

Next, we explore the role of $\mathcal{V}_U$: In order to have $\theta_e > 0$ we must require that the condition $\Delta(\eta_e; \beta, \mu, \nu, \eta_0, p) > 0 (\Leftrightarrow \mathcal{P}(\eta_e; \beta) > \mathcal{Q}(\eta_e; \mu, \nu, \eta_0, p))$. We first notice that $\Delta(\eta_e; \beta, \mu, \nu, \eta_0, p) \leq 0$ for $\eta_e \geq 1/\beta$. Next, let us introduce the set $\mathcal{D}_\Delta$ defined as

$$\mathcal{D}_\Delta = \{\eta_e; \quad \Delta(\eta_e; \beta, \mu, \nu, \eta_0, p) > 0, \quad 0 \leq \eta_e < 1/\beta\}. \tag{31}$$

We readily observe that the η-coordinates of the positive equilibrium points P_e belong to the subset $\mathcal{I}$ defined as

$$\mathcal{I} \equiv \mathcal{V}_U \cap \mathcal{D}_\Delta. \tag{32}$$

Now, by making use of (23) and (24) we end up with the equation

$$W(\eta_e) = 0, \tag{33}$$

in η_e where the function $W : \mathcal{I} \to \mathbb{R}$ is the composite function defined by

$$W(\eta_e) \equiv \big[I - U \circ V\big](\eta_e) = \eta_e - U(V(\eta_e)). \tag{34}$$

Here I is the identity mapping, i.e., $I(\eta_e) = \eta_e$. We conclude that if a positive equilibrium point P_e exists, then the η_e-coordinate of P_e satisfies (33)–(34) and is confined to the interval $\mathcal{I}$, where it is tacitly assumed that $\mathcal{I}$ is non-empty.

We start by using these constraints to derive the following non-existence results for equilibrium states:

- For $\mu \geq 1$, we find that the function V defined by means of (24) satisfies $V(\eta_e) \leq 0$ for all $\eta_e \geq 0$. This means that $\mathcal{D}_\Delta = \emptyset$ from which it follows that $\mathcal{I} = \emptyset$. Hence we have no interior equilibrium states in this case. Notice that this conclusion is exactly the same result as we got for the herbivore—biomass model investigated in Bergland et al. (2019).
- Let us consider the regime $0 \leq \mu < 1$. We fixate the Group 1 parameters (the herbivore parameters) to be given as for example in Table 3 and explore the issue of existence and non-existence of positive interior equilibrium points as a function of the normalized mortality rate of the top predators γ and the decimation parameter $\eta_{\max}$. The function Δ has at least one positive zero and maximum three positive zeros. These zeros are always strictly less than $1/\beta$. See also Appendix A In the phase plots in Fig. 3 we have identified regimes in the $\gamma, \eta_{\max}$-parameter plane for which we will not get positive equilibrium states: Red (green) coloured regions in the $\gamma, \eta_{\max}$-parameter plane correspond to $\Delta < 0$ ($\Delta > 0$). For a given $\gamma \in (0, 1/\beta)$, the interval $\mathcal{V}_U$ is represented by a line segment which is parallel to the $\eta_{\max}$-axis and which starts at the line $\eta_{\max} = \gamma$. Note that the condition $\eta_{\max} = \gamma$ models the situation with no harvesting of the top predators ($\epsilon = 0$). In that situation the decimation of this type of predators is only caused by the natural mortality. For line segments which are totally located in the red regions, we will get $\theta_e \leq 0$ by appealing to (24). Hence the interval $\mathcal{I}$ defined by means of (32) is empty. In this case we will have no positive equilibrium states. We also conclude that a necessary condition for the existence of positive equilibrium states is that parts of the vertical line segment corresponding to the interval $\mathcal{V}_U = [\gamma, \eta_{\max}]$ are located in the green sketched regions (which means that the interval $\mathcal{I}$ is non-empty). In this investigation we have chosen to use the Group 1 parameters in Table 3. Notice that Set A and Set B in Table 3 will give rise to line segments of the type labeled by A and B in Fig. 3b. For Set C, we get a vertical line segment of the type labeled with C in Fig. 3c. Finally, notice that the outcomes of Fig. 3 yield bounds on the coordinates of the possible positive equilibrium points.

In order to pursue the problem of detecting positive equilibrium points we must take into account the properties of the function Δ defined by means of (14), together with the results summarized in phase plots of the types demonstrated in Fig. 3.

Let us look at a scenario corresponding to the parameter regimes ($\beta > \beta_{cr}, Q_m > 1$) or ($\beta > \beta_{cr,2}, Q_m \leq 1$), which means that the function Δ has unique zero η^*. Assume that $\gamma < \eta^*$. In this case the subinterval $\mathcal{I}$ defined by means of (32) is non-empty. We readily find that

$$W(\gamma) = \gamma - U(V(\gamma)),$$
$$W(\eta_{\max}) = \eta_{\max} - U(V(\eta_{\max})),$$

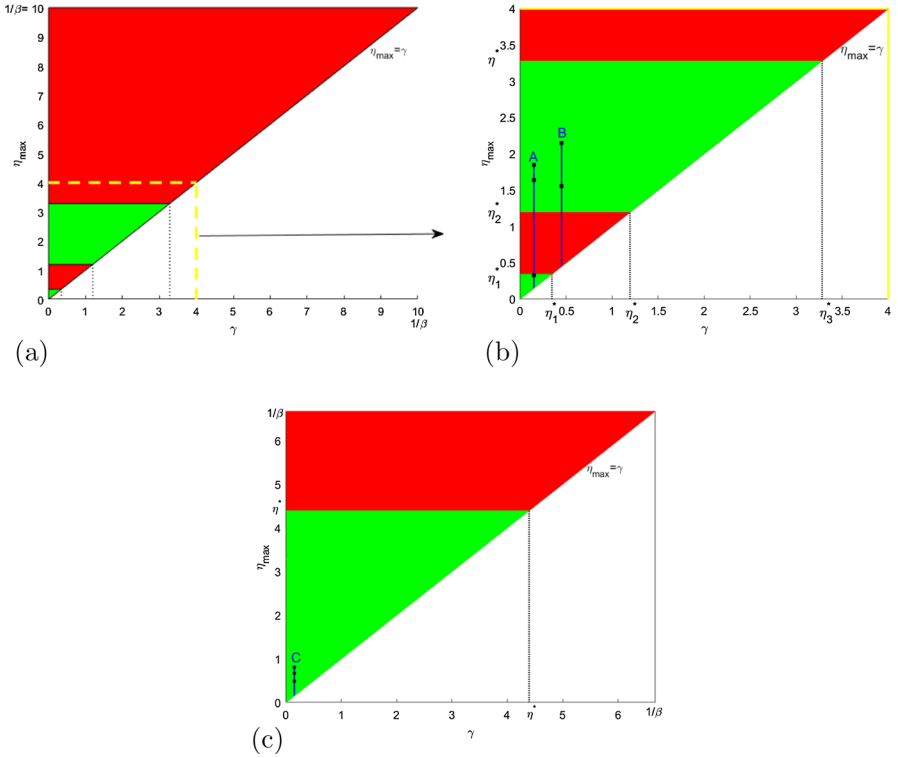

Fig. 3 Existence/non-existence of positive equilibrium states P_e as a function of $(\gamma, \eta_{\max}) \in \mathcal{B}_{A,B}$ where $\mathcal{B}_{A,B} \equiv \{(\gamma, \eta_{\max}) \in \mathbb{R}^2_+, \quad 0 \le \gamma \le 1/\beta, \gamma \le \eta_{\max} \le 1/\beta\}$. The input parameters are the herbivore (Group 1) parameters and $\mathcal{Q}_m$ in Set A and Set B in Table 3 for which η_1^*, η_2^* and η_3^* are given by (18). The set $\mathcal{B}_{A,B}$ is shown in (**a**). The phase plot in (**b**) is a magnified version of the subset of $\mathcal{B}_{A,B}$ with a yellow boundary curve. The interval $\mathcal{V}_U = [\gamma, \eta_{\max}]$ for Set A and Set B is represented by means of vertical line segments (blue color) of the type labeled with A and B in (**b**). The η-coordinates of the positive equilibrium points listed in Table 5 are marked with dots. **c** Existence/non-existence of positive equilibrium states P_e as a function of $(\gamma, \eta_{\max}) \in \mathcal{B}_C$ where $\mathcal{B}_C \equiv \{(\gamma, \eta_{\max}) \in \mathbb{R}^2_+, \quad 0 \le \gamma \le 1/\beta, \gamma \le \eta_{\max} \le 1/\beta\}$. The input parameters are the herbivore (Group 1) parameters and $\mathcal{Q}_m$ in Set C in Table 3 for which η^* is given by (19). The interval $\mathcal{V}_U = [\gamma, \eta_{\max}]$ for Set C is represented by means of vertical line segments (blue colour) of the type labeled with C. The η-coordinates of the positive equilibrium points listed in Table 5 are marked with dots. For further explanation, see the main text (Color figure online)

and that

$$W(\eta^*) = \eta^* - U(0) = \eta^* - \gamma > 0, \quad W(0) = -U(\varrho^{-1}(1-\mu)) < 0. \tag{35}$$

Since W is continuous, we will have $W(\eta_e) < 0$ for η_e in some interval about $\eta_e = 0$ and $W(\eta_e) > 0$ for η_e in some interval about $\eta_e = \eta^*$. The intermediate value theorem for continuous functions implies in this case that there is at least one $\eta_e^* \in \mathcal{I} = (\gamma, \eta_{\max})$ for γ close to zero and $\eta_{\max}$ close to η^* such that $W(\eta_e^*) = 0$. Next, let us address the uniqueness issue for the positive equilibrium states. Simple computation

reveals by using the chain rule that

$$\begin{aligned} W'(\eta_e) &= 1 - U'(V(\eta_e))V'(\eta_e) \\ &= 1 - \varrho^{-1}\epsilon\Phi'(V(\eta_e);\theta_0,k)\Delta'(\eta_e;\beta,\mu,\nu,\eta_0,p). \end{aligned} \tag{36}$$

We have made use of the fact that $\Delta'(\eta_e;\beta,\mu,\nu,\eta_0,p) = -\beta - \nu\Phi'(\eta_e;\eta_0,p)$. Hence, since $\Phi'(\eta_e;\eta_0,p) > 0$ on the interval $[0,\eta^*]$, $\Delta'(\eta_e;\beta,\mu,\nu,\eta_0,p) < 0$ on this interval. We also observe that the function V maps the interval $[0,\eta^*]$ onto the interval $[0,\frac{1}{\varrho}(1-\mu)]$. Thus, if $U'(\theta_e) \geq 0$ for all $0 \leq \theta_e \leq \frac{1}{\varrho}(1-\mu)$, we get that $W'(\eta_e) > 0$ on the interval $[0,\eta^*]$, which means that W is strictly increasing on this interval. We conclude that the equation (33) has a unique solution in the interval $(0,\eta^*)$.

Notice that this existence and uniqueness result for interior equilibrium states also holds true for the regimes $\mathcal{Q}_m > 1$, $0 < \beta < \beta_{cr}$ and $\mathcal{Q}_m < 1$, $\beta_{cr,1} < \beta < \beta_{cr,2}$ on the interval $[0,\eta_1^*]$ for which we have $\Phi'(\eta_e;\eta_0,p) > 0$ and $U'(\theta_e) \geq 0$ for all $0 \leq \theta_e \leq \frac{1}{\varrho}(1-\mu)$ and with γ close to zero and $\eta_{\max}$ close to η_1^*.

Let us next investigate a scenario for which we are in the regime $0 < \beta < \beta_{cr}$, $\mathcal{Q}_m > 1$ or in the regime $\beta_{cr,1} < \beta < \beta_{cr,2}$, $\mathcal{Q}_m \leq 1$. Assume that $\eta_2^* < \gamma < \eta_3^*$. In this case the interval $\mathcal{I}$ is non-empty, and we get

$$\begin{aligned} W(\eta_2^*) &= \eta_2^* - U(0) = \eta_2^* - \gamma < 0, \\ W(\eta_3^*) &= \eta_3^* - U(0) = \eta_3^* - \gamma > 0. \end{aligned}$$

The usage of the intermediate value theorem of continuous functions again shows that the function W has at least one zero in the open interval (η_2^*,η_3^*). For the limiting cases $\gamma \to \eta_2^*$ and $\eta_{\max} \to \eta_3^*$, we thus conclude that there is at least one positive equilibrium point P_e for which the η-coordinate is confined to the interval (η_2^*,η_3^*). This serves as the starting point for detecting positive equilibrium states P_e for which the η_e-coordinates belong to this interval.

In order to detect positive equilibrium states P_e in parameter regimes for which we theoretically cannot predict the existence of such states we resort solely on numerical simulations.

3.4 Stability of the Equilibrium Points

The vector field $\mathbf{F}$ defining the dynamical system (6) is given as

$$\mathbf{F}(\mathbf{x}) = \begin{bmatrix} r\zeta\theta\mathcal{H}(\theta,\eta,\xi;\gamma,\epsilon,\theta_0,k) \\ q\beta\eta\mathcal{G}(\theta,\eta,\xi;\varrho,\mu,\nu,\eta_0,p) \\ \xi\mathcal{F}(\theta,\eta,\xi;\beta) \end{bmatrix}, \quad \mathbf{x} = \begin{bmatrix} \theta \\ \eta \\ \xi \end{bmatrix}. \tag{37}$$

The Jacobian $D_{\mathbf{x}}\mathbf{F}$ of this vector field is given as

$$D_{\mathbf{x}}\mathbf{F} = \begin{bmatrix} r\zeta(\mathcal{H} + \theta\mathcal{H}_\theta) & r\zeta\theta\mathcal{H}_\eta & r\zeta\theta\mathcal{H}_\xi \\ q\beta\eta\mathcal{G}_\theta & q\beta(\mathcal{G} + \eta\mathcal{G}_\eta) & q\beta\eta\mathcal{G}_\xi \\ \xi\mathcal{F}_\theta & \xi\mathcal{F}_\eta & \mathcal{F} + \xi\mathcal{F}_\xi \end{bmatrix}, \tag{38}$$

where we for the sake of convenience use the abbreviations

$$\mathcal{H} \equiv \mathcal{H}(\mathbf{x};\, \gamma, \epsilon, \theta_0, k), \quad \mathcal{G} \equiv \mathcal{G}(\mathbf{x};\, \varrho, \mu, \nu, \eta_0, p), \quad \mathcal{F} \equiv \mathcal{F}(\mathbf{x};\, \beta)$$

and the short form notation

$$\mathcal{H}_\theta \equiv \frac{\partial \mathcal{H}}{\partial \theta}, \quad \mathcal{H}_\eta \equiv \frac{\partial \mathcal{H}}{\partial \eta} \quad \mathcal{H}_\xi \equiv \frac{\partial \mathcal{H}}{\partial \xi}, \quad \mathcal{G}_\theta \equiv \frac{\partial \mathcal{G}}{\partial \theta}, \quad \mathcal{G}_\eta \equiv \frac{\partial \mathcal{G}}{\partial \eta},$$
$$\mathcal{G}_\xi \equiv \frac{\partial \mathcal{G}}{\partial \xi}, \quad \mathcal{F}_\theta \equiv \frac{\partial \mathcal{F}}{\partial \theta}, \quad \mathcal{F}_\eta \equiv \frac{\partial \mathcal{F}}{\partial \eta}, \quad \mathcal{F}_\xi \equiv \frac{\partial \mathcal{F}}{\partial \xi},$$

for the partial derivatives. For the purpose of assessing the stability of the equilibrium points, we evaluate $D_{\mathbf{x}}\mathbf{F}$ at these points.

3.4.1 Stability of the Boundary Equilibrium Points

The Jacobian evaluated at the equilibrium point $P_0 = (0, 0, 0)$ is given as the diagonal matrix

$$D_{\mathbf{x}}\mathbf{F}(P_0) = \begin{bmatrix} -r\zeta\gamma & 0 & 0 \\ 0 & -q\beta\mu & 0 \\ 0 & 0 & 1 \end{bmatrix}. \tag{39}$$

The eigenvalues are $\lambda_1 = -r\zeta\gamma < 0, \lambda_2 = -q\beta\mu < 0$ and $\lambda_3 = 1 > 0$. We conclude that P_0 is always unstable.

For the equilibrium point $P_1 = (0, 0, 1)$ we get the Jacobian

$$D_{\mathbf{x}}\mathbf{F}(P_1) = \begin{bmatrix} -r\zeta\gamma & 0 & 0 \\ 0 & q\beta(1-\mu) & 0 \\ 0 & -\beta & -1 \end{bmatrix}, \tag{40}$$

with the eigenvalues $\lambda_1 = -r\zeta\gamma < 0$, $\lambda_2 = q\beta(1-\mu)$ and $\lambda_3 = -1 < 0$. Hence P_1 is asymptotically stable when $\mu > 1$ and unstable when $0 \leq \mu < 1$. The transition point $\mu = 1$ is static codimension 1 bifurcation point. The stability assessment based on linearization is inconclusive in this case.

Finally, we investigate the stability of the boundary equilibrium point P^*. Recall that equilibrium points of this type exist provided $0 \leq \mu \leq 1$. We readily find that the

Jacobian evaluated at this equilibrium point reads

$$D_{\mathbf{x}}\mathbf{F}(P^*) = \begin{bmatrix} r\zeta(\eta^* - \gamma) & 0 & 0 \\ -q\beta\eta^*\varrho & -q\beta\eta^*\nu\Phi'(\eta^*;\eta_0,p) & q\beta\eta^* \\ 0 & -\beta\xi^* & -\xi^* \end{bmatrix}, \tag{41}$$

where γ is defined by (26). The eigenvalues of $D_{\mathbf{x}}\mathbf{F}(P^*)$ are given by

$$\left.\begin{aligned} \lambda_1 &= r\zeta(\eta^* - \gamma), \\ \lambda_\pm &= \frac{1}{2}\big[tr(\mathbb{J}_2) \pm \sqrt{(tr(\mathbb{J}_2))^2 - 4det(\mathbb{J}_2)}\big], \end{aligned}\right\} \tag{42}$$

where $\mathbb{J}_2$ is the 2×2-matrix

$$\mathbb{J}_2 = \begin{bmatrix} -q\beta\eta^*\nu\Phi'(\eta^*;\eta_0,p) & q\beta\eta^* \\ -\beta\xi^* & -\xi^* \end{bmatrix}. \tag{43}$$

Note that $\mathbb{J}_2$ is the stability matrix derived in Bergland et al. (2019) for the purpose of assessing the linear stability of the equilibrium states (η^*, ξ^*). Based on (3.4.1) we arrive at the following conclusions regarding the stability of the boundary point P^*:

- If $\gamma < \eta^*$, we find that $\lambda_1 > 0$ from which it follows that P^* is unstable.
- If $\gamma > \eta^*$, we will have $\lambda_1 < 0$. In this case the stability properties of P^* can be inferred directly from the stability analysis of the equilibrium states (η_*, ξ_*).
- The transition state $\gamma = \eta^*$ corresponds to a non-hyperbolic equilibrium point $P^* = (0, \gamma, 1 - \beta\gamma)$ for which the stability assessment based on the linearization procedure is not applicable. We do not pursue a detailed analysis of this state.

We have summarized the stability properties of the three equilibrium points P_1^*, P_2^* and P_3^* as a function of the normalized mortality parameter γ in Fig. 4a for the cases $\mathcal{Q}_m > 1, 0 < \beta < \beta_{cr}$ and $\mathcal{Q}_m \leq 1, \beta_{cr,1} < \beta < \beta_{cr,2}$.

3.4.2 Stability Assessment of the Positive Interior Equilibrium Points

The stability assessment of a positive interior equilibrium point $P_e = (\theta_e, \eta_e, \xi_e)$ proceeds in the following way:

- Compute $W'(\eta_e)$ given by (36). If $W'(\eta_e) < 0$, P_e is unstable, see Theorem 1 in Appendix C.
- Assume $W'(\eta_e) > 0$. Then the stability assessment is based on the Routh–Hurwitz criterion (or equivalently direct exploration of the spectral properties of the corresponding Jacobian $D_{\mathbf{x}}\mathbf{F}(P_e)$). According to Theorem 2 in Appendix C, the positive equilibrium state $P_e = (\theta_e, \eta_e, \xi_e)$ is asymptotically stable if θ_e, η_e satisfies the bounding inequalities

$$0 < \theta_e \leq (k-1)^{1/k}\theta_0, \quad 0 < \eta_e \leq (p-1)^{1/p}\eta_0. \tag{44}$$

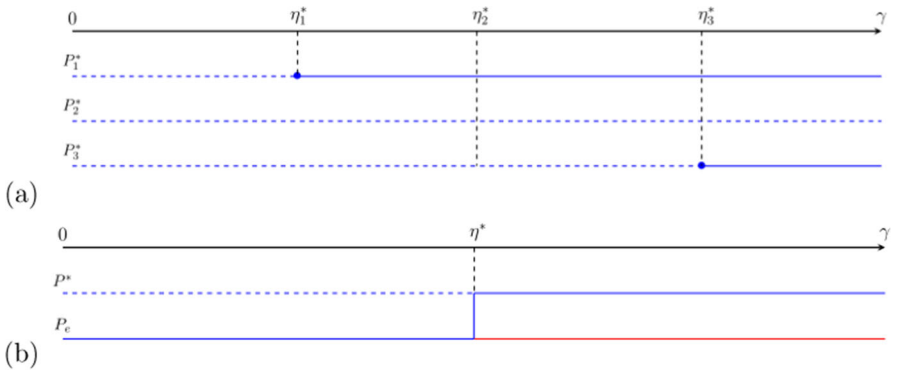

Fig. 4 **a** Summary of the stability properties of the three boundary equilibrium states P_1^*, P_2^* and P_3^* as a function of the normalized mortality parameter γ. Dotted lines correspond to unstable equilibrium points, whereas bold line means asymptotically stable equilibrium points. The parameter regimes are $0 < \beta < \beta_{cr}$, $Q_m > 1$ and $\beta_{cr,1} < \beta < \beta_{cr,2}$, $Q_m \leq 1$. Here η_1^*, η_2^* and η_3^* are the three zeros of the function Δ. **b** Summary of the properties of the existence and stability of the equilibrium states P^* and P_e as a function of the normalized mortality parameter γ in the regimes $\beta > \beta_{cr}$, $Q_m > 1$ and $\beta > \beta_{cr,2}$, $Q_m \leq 1$. Here η^* is the unique zero of the function Δ. Blue bold lines represent asymptotically stable equilibrium points, blue dashed line represents unstable equilibrium points, whereas red bold line represents non-existence of equilibrium points (Color figure online)

Notice that the bounding inequalities in (44) are a sufficient condition for the asymptotic stability of the corresponding interior equilibrium point P_e. However, it does not a provide a necessary condition for asymptotic stability. Thus an interior equilibrium point P_e can be asymptotically stable even if the condition (44) is violated.

Notice that we will have $P_e \to P^* = (0, \eta^*, 1 - \beta\eta^*)$ and $D_{\mathbf{x}}\mathbf{F}(P_e) \to D_{\mathbf{x}}\mathbf{F}(P^*)$ when $\gamma \to \eta^*$. This limit represents a non-hyperbolic equilibrium point for which one of the eigenvalues of the Jacobian $D_{\mathbf{x}}\mathbf{F}(P^*)$ is 0. A stability assessment based on spectral properties of this Jacobian is not applicable. For the case $\beta + \nu\Phi'(\eta^*; \eta_0, p) < 0$ (corresponding to $\Delta'(\eta^*; \beta, \mu, \nu, \eta_0, p) > 0$), one of the eigenvalues is strictly positive. According to Shoshitaishvilis theorem, the actual non-hyperbolic point P^* is unstable in this case.[4] We do not pursue any further analysis of the stability problem for the non-hyperbolic case corresponding to $\beta + \nu\Phi'(\eta^*; \eta_0, p) > 0$.

The generic picture which emerges in the parameter regimes $0 \leq \mu < 1$, $\gamma < \eta^*$ when $\mathcal{Q}_m > 1$, $\beta > \beta_{cr}$ and $\mathcal{Q}_m \leq 1$, $\beta > \beta_{cr,2}$ is the existence of a unique boundary equilibrium point P^*. The situation can be described as follows: For $\gamma < \eta^*$, the boundary equilibrium points P_0, P_1 and P^* are all unstable. Moreover, let us assume that we have an interior positive equilibrium point P_e for which the θ_e-and the η_e-coordinates satisfy the bounding inequalities (44). This equilibrium state is asymptotically stable. When $\gamma \to \eta^*$, P_e merges together with P^*, where the limiting equilibrium point becomes non-hyperbolic. For the case $\gamma \geq \eta^*$, P_0 and P_1 remain unstable, whereas P^* is converted to an asymptotically stable equilibrium point. In this regime no positive interior equilibrium points P_e ceases to exist. Figure 4b summarizes

[4] See for example Chapter 6 in Arnold (1988)

Table 5 Coexistence and stability of boundary and positive equilibrium points as a function of the input parameter sets in Table 3

Parameters	Equilibrium point	θ_e	η_e	ξ_e	Stability
Set A	P_1^*	0	0.3462	0.9654	Unstable
	P_2^*	0	1.1955	0.8805	Unstable
	P_3^*	0	3.2812	0.6719	Unstable
	$P_{e,1}$	0.1386	0.3326	0.9667	Asymptotically stable
	$P_{e,2}$	0.2151	1.6413	0.8359	Unstable
	$P_{e,3}$	0.2469	1.8584	0.8142	Asymptotically stable
Set B	P_1^*	0	0.3462	0.9654	Asymptotically stable
	P_2^*	0	1.1955	0.8805	Unstable
	P_3^*	0	3.2812	0.6719	Unstable
	$P_{e,2}$	0.1928	1.5578	0.8442	Unstable
	$P_{e,3}$	0.2455	2.1557	0.7844	Asymptotically stable
Set C	P_1^*	0	4.3930	0.3411	Unstable
	$P_{e,1}$	0.1814	0.4961	0.9256	Asymptotically stable
	$P_{e,2}$	0.2040	0.6792	0.8981	Unstable
	$P_{e,3}$	0.2768	0.8226	0.8766	Unstable

Notice that we here use the notation η_e and ξ_e for the coordinates of the boundary equilibrium points (instead of η^* and ξ^*). For the boundary equilibrium points the stability assessment is based on the eigenvalues (42) of the Jacobian (41), and the subsequent stability discussion

the stability properties of P^* and the existence and stability properties of P_e as a function of the normalized mortality rate γ.

The modelling framework also permits more complex scenarios such as coexistence of boundary equilibrium points and positive interior equilibrium points. In the remaining part of the present paper we will give examples of such scenarios. Table 5 contains numerical examples of this coexistence problem together with the stability properties of the detected equilibrium states. The input parameters underlying the computations leading to these results are given as Set A, Set B and Set C in Table 3. For the Set A, the ordering of the boundary equilibrium points $P_i^* = (0, \eta_i^*, \xi_i^*)$ and the positive interior equilibrium points $P_{e,i} = (\theta_{e,i}, \eta_{e,i}, \xi_{e,i})$ satisfies $\gamma < \eta_{e,1} < \eta_1^* < \eta_m < \eta_2^* < \eta_{e,2} < \eta_{e,3} < \eta_{\max} < \eta_3^*$. For Set B we get the ordering $\eta_1^* < \gamma < \eta_m < \eta_2^* < \eta_{e,2} < \eta_{e,3} < \eta_{\max} < \eta_3^*$, whereas for Set C we have $\gamma < \eta_{e,1} < \eta_m < \eta_{e,2} < \eta_{e,3} < \eta_{\max} < \eta_1^* \equiv \eta^*$, see the phase plots in Fig. 3. The outcome regarding the stability analysis is also given in Table 5.

Remark 2 Noticing that $\eta_m \equiv (p-1)^{1/p}\eta_0 = 0.526$ and $\theta_m \equiv (k-1)^{1/k}\theta_0 = 0.255$ for the input parameters in Table 3, we have made use of the bounding inequalities (44) (see Theorem 2 in Appendix C) to prove that the positive interior equilibrium point $P_{e,1}$ (for Set A and Set C) is asymptotically stable. The asymptotic stability of $P_{e,3}$ for Set A and Set B follows from direct numerical computation of the eigenvalues of the corresponding Jacobian (C6): The real part of all these eigenvalues is strictly negative. The negativity of the constant term a_3 in the characteristic polynomial (C8)

(see Theorem 1 in Appendix C) implies instability of the positive interior equilibrium points $P_{e,2}$ (for Set A and Set C), whereas the instability of $P_{e,2}$ (for Set B) and $P_{e,3}$ (for Set C) is shown by direct numerical exploration of the spectral properties of the corresponding Jacobian (C6). Here we notice that we do not cover all possible equilibrium and stability scenarios for the present modelling framework.

Remark 3 The global stability issue can be resolved provided one manages to construct a Liapunov function of a special form, which serves as a sufficient condition for the global stability problem. To extend the local asymptotically stability results of interior equilibrium points in our model to global results is a challenging problem, however. Several factors have to be taken into account: First of all, the number of interior equilibrium points and their respective stability properties turn out to be complicated functions of the input parameters. Each stable equilibrium state of this type divides the phase space into different attractor basins, which means that the existence of globally stable equilibrium state is precluded. Even in the case of a unique stable interior equilibrium point a necessary condition for this equilibrium state to be globally stable is the absence of asymptotically stable boundary equilibrium points. The analytical results and the numerical simulation reveal that the existence and the stability of equilibrium points as a function of the input parameters is a rather complicated issue. We do not pursue this stability issue here, however.

4 Equilibrium States and Dynamical Evolution

In this section we detail the dynamical evolution of the system (6) in the first orthant of the phase space numerically. We use Set A and Set B in Table 3 as input parameters in these simulations except that we vary the normalized mortality rate μ. The focus here is on the role of the detected equilibrium points and their respective stability properties in the dynamical evolution. As we have no interior equilibrium points for $\mu \geq 1$, whereas we for the complementary case $0 \leq \mu < 1$ have detected such equilibrium states, we treat these two cases separately (Sects. 4.1 and 4.2).

4.1 The High Herbivore Mortality Regime: $\mu \geq 1$

We first detail numerically the temporal evolution of the state variables θ, η and ξ when the normalized mortality rate μ of the herbivores is greater than 1. According to Sect. 3.3.1 this means that we are investigating a regime for which the only equilibrium points are given as $P_0 = (0, 0, 0)$ and $P_1 = (0, 0, 1)$. We restrict ourselves to Set A in Table 3 as input parameters in these simulations except that we increase μ to be given as $\mu = 1.1$. The outcome of the numerical run which is summarized in Fig. 5, show that the integral curve of the governing system settles down on the asymptotically stable equilibrium state P_1, after an initial transient phase. We have also carried out numerical runs using Set B and Set C in Table 3 as input parameters. These runs all show the same feature as in Fig. 5. We therefore conjecture that any integral curve starting in the first orthant of the phase space will finally be attracted towards the asymptotically stable equilibrium point P_1. By restoring to the dimensional variables

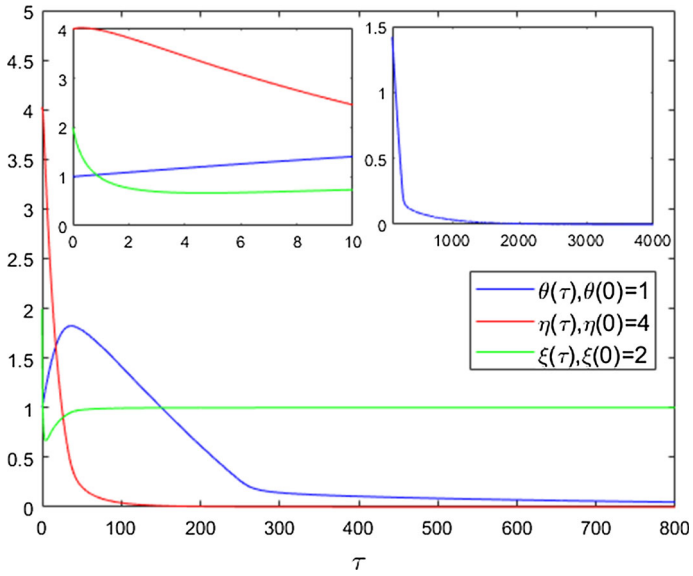

Fig. 5 Integral curves of the system (6)–(7) in the case of high mortality rate for the herbivores. Parameter set A in Table 3, except for $\mu = 1.1$

and parameters we conclude that the herbivores and the top predators go extinct in this case whereas the biomass approaches the carrying capacity K.

4.2 The Low and Moderate Herbivore Mortality Regime: $0 \leq \mu < 1$

We next examine the regime $0 \leq \mu < 1$. The analysis of the existence of equilibrium states and their respective stability properties in the previous subsection shows that the modelling framework possesses a rich and complex variety of dynamical phenomena. In this subsection we will detail numerically the dynamical evolution of the state variables when the input parameters in our computations are given as Set A and Set B in Table 3. Set A generates two stable interior equilibrium states, whereas all boundary equilibrium states without top predators are unstable. Set B generates one stable interior equilibrium states, and one stable boundary equilibrium state.

We consider a sequence of time dependent outcomes when using the Set A in Table 3 as input parameters. The results of this investigation are summarized in Fig. 6. This figure shows the evolution of the population densities for different initial condition. For Fig. 6a we have selected as initial condition a perturbation in the θ-direction of the unstable boundary equilibrium point P_2^*, whereas for Fig. 6b we have chosen the initial condition as a perturbation in the θ-direction of the unstable boundary equilibrium point P_3^*. In both cases we observe that in the final stage we get a saturation of all the population levels at a level given by the asymptotically stable equilibrium state $P_{e,1}$. The first phase of the development in Fig. 6a consists of plateaus in all the population densities. In the next phase we observe an increase in the top predator level accompanied by a significant decimation of the herbivore population. The biomass

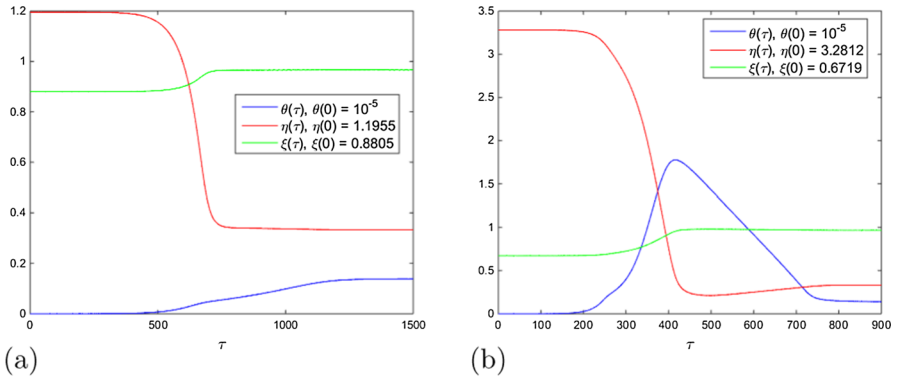

Fig. 6 Integral curves of the system (6)–(7), for Set A in Table 3 as input parameters, are attracted towards the interior equilibrium point $P_{e,1} = (0.1386, 0.3326, 0.9667)$. **a** The initial condition is given as a perturbation of the unstable equilibrium point P_2^* in the θ-direction. **b** The initial condition is given as a perturbation of the unstable equilibrium point P_3^* in the θ-direction

level experiences a slight increase in this phase. In the final stage we get a saturation of all the population levels at a level given by the asymptotically stable equilibrium state $P_{e,1}$. In Fig. 6b we again observe a plateau formation in the initial stage of the development of all the population levels. The intermediate phase starts with a slow growth in top predator level together with a decrease in the herbivore level. Moreover, in this phase we observe a significant growth and formation of a peak in the top predator population level together with a rapid decrease in the herbivore population. When the top predators density decreases, the herbivore population will experience a modest increase before it saturates on a constant level. The decrease in herbivore level is accompanied by a slow growth in the biomass which finally settles down on a constant level. The final stage thus consists of a stabilization at population levels which are determined by the asymptotically stable equilibrium $P_{e,1}$. We conclude that the unstable equilibrium points P_2^* and P_3^* both belongs to the attraction basin of $P_{e,1}$.

Next, we investigate some numerical outcomes when using Set B in Table 3 as input parameters. In Fig. 7a we have chosen an initial condition in the vicinity of of the unstable boundary equilibrium point P_2^* characterized by a small perturbation in the θ-coordinate. We observe a plateau formation in the initial phase of the herbivore- and the biomass level, before the stabilization sets in in the next phase. The latter phase is characterized by a lower herbivore level and a slightly higher level in the biomass density. A notable feature in the initial phase is that the top predator level grows and attains a maximum before it slowly decays to the zero level, which means that the top predators go extinct. We observe that the top predator level will be very small as compared to the herbivore-biomass level in this process. The final stabilizing level is determined by the asymptotically stable boundary equilibrium point P_1^*.

In Fig. 7b we demonstrate the numerical outcome when selecting the initial condition as a perturbation of the equilibrium point P_3^* in the θ-direction. Initially we get a short plateau formation phase in all the population densities, followed by a phase where we get a sharp drop in the herbivore level to a lower saturating level. The biomass

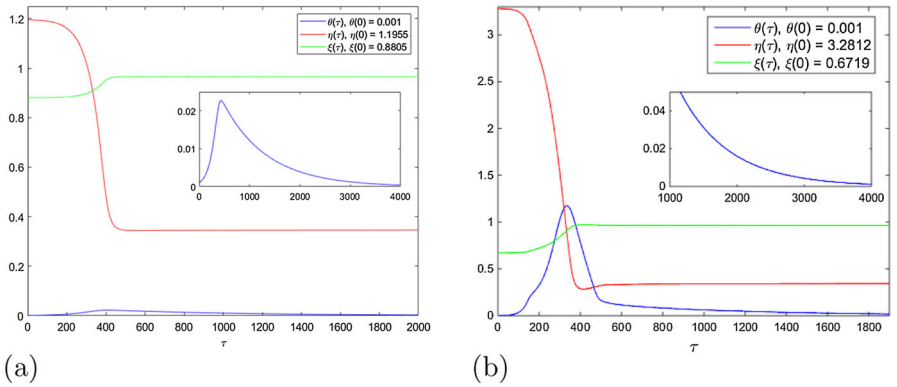

Fig. 7 Integral curves of the system (6)–(7), for Set B in Table 3 as input parameters, are attracted towards the asymptotically stable boundary equilibrium point $P_1^* = (0, 0.3462, 0.9654)$, see Table 5. **a** The initial condition is given as a perturbation of the unstable equilibrium point P_2^* in the θ-direction. **b** The initial condition is given as a perturbation of the unstable equilibrium point P_3^* in the θ-direction

exhibits a moderate increase before it saturates at a higher level. Interestingly, the top predator level increases and attains a maximum in this second intermediate phase and then decreases slowly to zero. The final saturating levels of the population densities are determined by the asymptotically stable boundary equilibrium point P_1^*.

From Fig. 7 we conclude that the unstable equilibrium points P_2^* and P_3^* both belongs to the attraction basin of P_1^*. Moreover, we compare the evolution shown in Fig. 6 with the evolution shown in Fig. 7, where the only difference consists of a higher natural mortality of top predators for Set B compared to Set A. The initial conditions used in the numerical runs are the same for both figures, i.e., as a perturbation of the equilibrium points P_2^* and P_3^* in the θ-direction. For the outcome of Set A (depicted in Fig. 6) we get a saturation level given by the asymptotically stable interior equilibrium state $P_{e,1}$ which means that the top predators survive. Assuming increased mortality of the top predators as given in Set B (with the outcome depicted in Fig. 7), we get a saturation given by the asymptotically stable boundary equilibrium state P_1^* which means an extinction of the top predators.

5 Local Structural Stability in the Limit $\epsilon \to 0$, Hopf- and Saddle Node Bifurcations

A notable feature of the herbivore part of the input parameters listed in Set C in Table 3 is a lower normalized herbivore mortality rate μ as compared with Set A and Set B in Table 3. We have shown that this leads to a scenario with one boundary equilibrium point and three interior equilibrium point, see Table 5. In this section we also use Set C as input parameters, except that we will vary the decimation parameters γ and ϵ for the top predators. We will focus on the dynamical output as a function of these two parameters. We study the local structural stability of our modelling framework in the limit $\epsilon \to 0$ (Sect. 5.1) as well the occurrence of Hopf bifurcations using

the normalized mortality rate γ as a control parameter (Sect. 5.2). In the numerical exploration of these phenomena we vary γ and permit ϵ to be small.

5.1 The Asymptotic Limit $\epsilon \to 0$: Weak Top Predator Taxation

The condition $0 \leq \epsilon \ll 1$ translates into the parameter regime $L_{\max} \ll rcK^2$ when restoring to the dimensional parameters, see Table 2. This means that the saturated maximal harvesting rate of the top predators, $L_{\max}$, is much smaller than the reference harvesting rate rcK^2. The regime $0 \leq \epsilon \ll 1$ is in accordance with (8) also of particular interest when implementing a wildlife management strategy for protection of carnivore populations where $L_{\max} \ll H_{\max}$.

This serves as a motivation for a study of the dynamical features in the regime $0 \leq \epsilon \ll 1$. The modelling framework (6)–(7) can be decomposed to the vector form as

$$\frac{d\mathbf{x}}{d\tau} = \mathbf{F}_0(\mathbf{x}) + \epsilon \mathbf{F}_1(\mathbf{x}), \quad \mathbf{x} = \begin{bmatrix} \theta \\ \eta \\ \xi \end{bmatrix}, \tag{45}$$

where the vector fields $\mathbf{F}_0$ and $\mathbf{F}_1$ are given as

$$\begin{aligned} \mathbf{F}_0(\mathbf{x}) &= \begin{bmatrix} r\zeta\theta\mathcal{H}_0(\theta,\eta,\xi;\gamma) \\ q\beta\eta\mathcal{G}_0(\theta,\eta,\xi;\varrho,\mu,\nu,\eta_0,p) \\ \xi\mathcal{F}_0(\theta,\eta,\xi;\beta) \end{bmatrix}, \\ \mathbf{F}_1(\mathbf{x}) &= \begin{bmatrix} r\zeta\theta\mathcal{H}_1(\theta,\eta,\xi;\theta_0,k) \\ 0 \\ 0 \end{bmatrix}. \end{aligned} \tag{46}$$

Here the component functions $\mathcal{H}_0$, $\mathcal{H}_1$, $\mathcal{G}_0$ and $\mathcal{F}_0$ are given as

$$\left.\begin{aligned} &\mathcal{H}_0(\theta,\eta,\xi;\gamma) \equiv \eta - \gamma, \quad \mathcal{H}_1(\theta,\eta,\xi;\theta_0,k) \equiv -\Phi(\theta;\theta_0,k), \\ &\mathcal{G}_0(\theta,\xi,\eta;\varrho,\mu,\nu,\eta_0,p) \equiv \xi - \varrho\theta - \mu - \nu\Phi(\eta;\eta_0,p), \\ &\mathcal{F}_0(\theta,\eta,\xi;\beta) \equiv 1 - \xi - \beta\eta. \end{aligned}\right\} \tag{47}$$

We aim at studying the asymptotic approximation of the solutions to (45) as $\epsilon \to 0$. This problem can be dealt with by means of the theory for regularly perturbed dynamical systems, see for example Vasil'eva et al. (1995). This means that we can approximate these solutions with the solutions of the simplified system

$$\frac{d\mathbf{x}}{d\tau} = \mathbf{F}_0(\mathbf{x}), \tag{48}$$

in this asymptotic limit for some τ-interval about $\tau = 0$. As the perturbation term $\mathbf{F}_1(\mathbf{x})$ is uniformly bounded from below and above, we will get a uniform asymptotic approximation for all $\tau > 0$.

The system (48) possesses the same boundary equilibrium points as (45). The corresponding stability properties are also the same. Notice that the interior positive equilibrium points are given as the 1-parameter family of points

$$\left.\begin{aligned} &P_e(\epsilon = 0) = (\theta_e(\gamma), \eta_e(\gamma), \xi_e(\gamma)), \\ &\theta_e(\gamma) \equiv \varrho^{-1}\Delta(\gamma; \beta, \mu, \nu, \eta_0, p), \quad \eta_e(\gamma) \equiv \gamma, \quad \xi_e(\gamma) \equiv 1 - \beta\gamma, \end{aligned}\right\} \tag{49}$$

parameterized by γ. Here the function Δ is defined by means of (14). The limiting result (49) is obtained by observing that $\eta_{\max} \to \gamma$ as $\epsilon \to 0$. This means that the interval $\mathcal{V}_U$ defined by means of (28) collapses to the single point γ in this limit. The positivity requirement imposed on θ_e and ξ_e implies that $\gamma \in \mathcal{D}_\Delta = \mathcal{I}$, where $\mathcal{D}_\Delta$ is defined as (31). The problem of determining the set $\mathcal{D}_\Delta$ is resolved by using the methodology elaborated in Appendix A The key problem here is to determine the number of zeros of Δ as a function of β. We also observe that the limiting system (48) has a unique interior equilibrium point of the type (49) in the limit $\epsilon \to 0$. This means that we will not have coexistence of several positive interior equilibrium points such as demonstrated for Set A—Set C in Table 3 (finite ϵ cases), see Table 5. This is consistent with the phase plots in Fig. 3. [5] Assume that $\gamma > 0$. The stability analysis of the interior equilibrium points of the type (49) proceeds by using the Routh–Hurwitz criterion in Appendix C with $B = 0$. We first observe that the coefficient a_3 in the characteristic polynomial $\mathcal{P}_3$ defined by (C8) is strictly positive when $\epsilon = 0$. This means that we always have a negative real eigenvalue of the Jacobian (C6). Theorem 2 implies that the interior equilibrium point is asymptotically stable if $\Phi'(\gamma; \eta_0, p) \geq 0$ ($\Leftrightarrow 0 < \gamma \leq (p-1)^{1/p}\eta_0$). For the complementary regime, i.e., when $\Phi'(\gamma; \eta_0, p) < 0$, the stability assessment is based on a direct exploration of the spectral properties of the Jacobian (C6). Notice that the interior equilibrium points merge together with the boundary equilibrium points when γ is set equal to one of the zeros of the function Δ and that they become non-hyperbolic equilibrium points in this case.

Let us consider an equilibrium point of the type (49) which is assumed to be hyperbolic. In that case the perturbed system (45) possesses an equilibrium point which appears as a smooth ϵ-deformation of the equilibrium point P_e ($\epsilon = 0$) and which also is hyperbolic. Then Hartman–Grobmans theorem implies that the unperturbed system (48) is locally structural stable in the vicinity of that point. The same holds true for the perturbed system (45). The phase portrait of the perturbed system (45) in the vicinity of the perturbed equilibrium point is mapped one- to -one and onto the phase portrait of the unperturbed system (48) in the vicinity of P_e ($\epsilon = 0$). See Guckenheimer and Holmes (1983) for details concerning the general exposition of the theory for hyperbolic equilibrium points and local structural stability.

[5] Notice also that we get an additional boundary equilibrium

$$P_*(\epsilon = 0) = (\varrho^{-1}(1 - \mu), 0, 1) \tag{50}$$

when $\epsilon = \gamma = 0$. Here we tacitly assume that $0 \leq \mu \leq 1$. We readily find that the characteristic polynomial $\mathcal{P}_3$ given by (C8) simplifies to $\lambda^3 + \lambda$ in this case, from which it follows that $P_*(\epsilon = 0)$ is subject to a degenerate bifurcation. We do not pursue any further theoretical analysis of this bifurcation here, however.

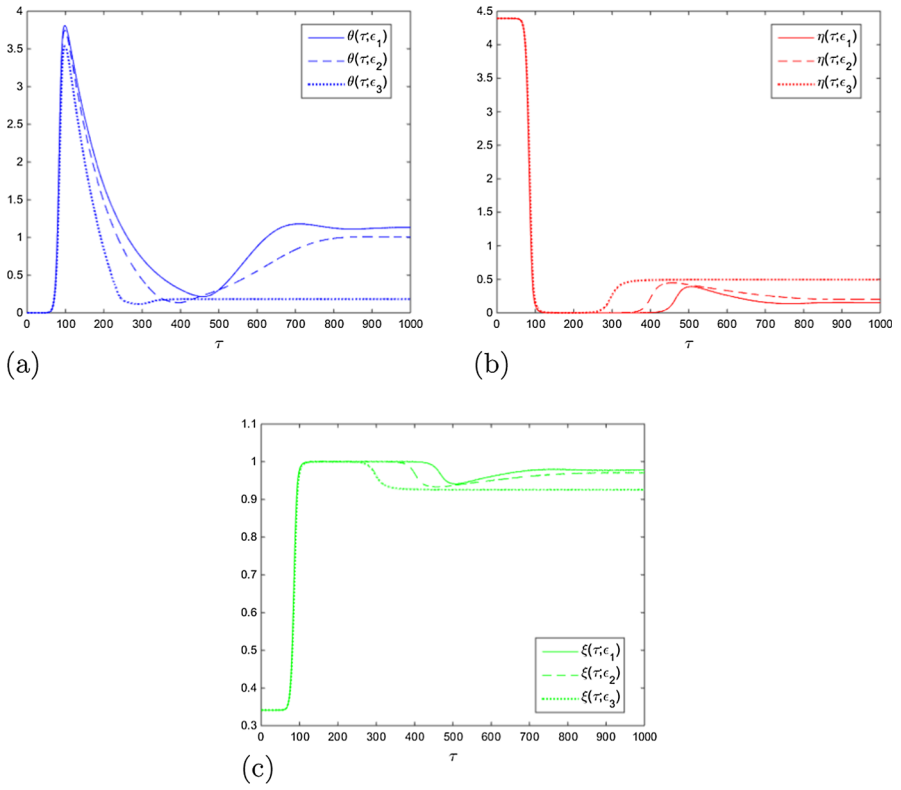

Fig. 8 Integral curves of the system (6)–(7) for different values of ϵ. **a** The top predator density θ (blue), **b** the herbivore density η (red) and **c** the biomass density ξ (green) in the regime $0 \leq \epsilon \ll 1$ ($\epsilon_1 = 0, \epsilon_2 = 0.05, \epsilon_3 = 0.2$). Input data: Set C in in Table 3 except for ϵ which is varied. Initial condition is close to the unstable boundary equilibrium point P_1^*: $\theta(0) = 10^{-8}$, $\eta(0) = 4.3930$ and $\xi(0) = 0.3411$, see Table 5 (Color figure online)

The numerical simulations confirming this prediction are summarized in Fig. 8. The input parameters underlying the numerical computations leading to this figure are given by all the parameters in Set C in Table 3 except for ϵ which is varied. In the present simulations we have chosen $\epsilon = 0, \epsilon = 0.05$ and $\epsilon = 0.2$. The initial condition selected is a perturbation in the θ-direction of the unstable boundary equilibrium point P_1^* for all the numerical runs. We readily observe that the ($\epsilon = 0.05$)-integral curve is closer to the ($\epsilon = 0$)-integral curve than the ($\epsilon = 0.2$)-curve. Moreover, the ($\epsilon = 0$)-integral curve stagnates at the asymptotically stable interior equilibrium point characterized by a lower herbivore density, a higher top predator density and a higher level of biomass as compared with the levels given by P_1^*. In the initial stage we see that both the top predators and the herbivores attain maximum levels accompanied by a depletion of the biomass. In this stage the increased herbivore density is subsequently followed by a top predator growth. The next phase is characterized by the herbivore population reaching a maximum before a significant decimation takes place, and a subsequent similar top predator depletion and a biomass growth. We observe that in all these regimes of top predator harvesting rate, the herbivore population almost goes

extinct, followed by a depletion of the top predator population. Furthermore, in the regime of no top predator harvesting rate ($\epsilon = 0$), the duration of an almost extinct herbivore population approximately doubles in time compared to what takes place in the regime $\epsilon = 0.2$. After this depletion phase we reach a final stage where all the three integral curves eventually settle down on the final stabilizing level. A notable feature is that the final stabilizing level of the top predators and biomass (herbivores) decreases (increases) with ϵ.

5.2 Hopf Bifurcations When $\epsilon = 0$

We finally investigate the possibility of having Hopf bifurcations in the simplified system (48). We assume that we are working in the parameter regime $0 \leq \mu < 1$, $\mathcal{Q}_m < 1$ and $0 < \beta < \beta_{cr,1}$ which means that we have a unique boundary equilibrium point of the type $P^* = (0, \eta^*, 1 - \beta\eta^*)$ for which $-\beta < \nu\Phi'(\eta^*; \eta_0, p) < 0$ ($\Leftrightarrow$ $\Delta'(\eta^*; \beta, \mu, \nu, \eta_0, p) < 0$). In this case the set of admissible values of γ producing positive interior equilibrium points is given by the interval $\mathcal{D}_\Delta = (0, \eta^*)$. The stability analysis summarized in (42) shows that the boundary equilibrium point P^* is unstable. We pursue the bifurcation problem in the following way: According to Shen and Jing (1995) and Appendix B in Nordbø et al. (2007) we translate the Hopf bifurcation problem into a study of the violation of the Routh - Hurwitz criterion. Viewing γ as a control parameter, we observe that the Routh–Hurwitz determinants defined by means of (C7)–(C12) (with $B = 0$ ($\Leftrightarrow \epsilon = 0$)) are smooth functions of γ. For $0 < \gamma \leq \eta_m$, Theorem 2 implies that $P_e(\epsilon = 0)$ is asymptotically stable. Let us next investigate the complementary regime $\eta_m \leq \gamma < \eta^*$. We proceed by evaluating the Routh - Hurwitz determinant $|D_1|$ at the points $\gamma = \eta_m$ and $\gamma = \eta^*$ and find that

$$|D_1|(\eta_m) = 1 - \beta\eta_m > 0, \tag{51}$$

$$|D_1|(\eta^*) = q\nu\beta\eta^*\Phi'(\eta^*; \eta_0, p) + 1 - \beta\eta^*. \tag{52}$$

By taking into account the fact that $0 < q < 1$, we readily find that

$$q\nu\beta\eta^*|\Phi'(\eta^*; \eta_0, p)| \leq \nu|\Phi'(\eta^*; \eta_0, p)| \leq \frac{\nu}{(\eta^*)^2} = \mathcal{O}(\beta^2).$$

Thus, we conclude that $q\nu\beta\eta^*|\Phi'(\eta^*; \eta_0, p) \ll 1 - \beta\eta^*$ for large η^* (or equivalently small β). This means that $|D_1|(\eta^*) > 0$ in the shallow β-regime we consider. As $\eta^* > \eta_m$, we will have $|D_1|(\eta^*) < |D_1|(\eta_m)$ in this regime.

Next, let us compute the Routh–Hurwitz determinant $|D_2|$ at the points $\gamma = \eta_m$ and $\gamma = \eta^*$. This computation yields

$$|D_2|(\eta_m) = q\beta^2\eta_m(1 - \beta\eta_m)^2 > 0, \tag{53}$$

$$|D_2|(\eta^*) = -q\beta\eta^*(1 - \beta\eta^*)\Delta'(\eta^*; \beta, \mu, \nu, \eta_0, p)|D_1|(\eta^*) \tag{54}$$

when also taking into account the expression (52) for $|D_1|(\eta^*)$ and the expression for $\Delta'(\eta^*; \beta, \mu, \nu, \eta_0, p)$ where Δ is defined as (14). Since $|D_1|(\eta^*) > 0$ in the shallow

β-regime and $\Delta'(\eta^*;\beta,\mu,\nu,\eta_0,p) < 0$, we conclude that $|D_2|(\eta^*) > 0$ in that β-regime. We conclude that the graph of the Routh–Hurwitz determinant $|D_2|$ as a function of γ in the generic case has either no intersection points with the γ-axis or an even number of transversal intersection point with this axis for $\gamma \in (\eta_m, \eta^*)$. We will demonstrate this feature numerically in what follows.

We finally observe that the constant term a_3 of the characteristic polynomial (C8) is given by

$$a_3 = r\zeta q\beta\gamma\Delta(\gamma;\beta,\mu,\nu,\eta_0,p)(1-\beta\gamma), \tag{55}$$

for the equilibrium (49), from which it follows that $a_3 > 0$ when $\epsilon = 0$. Hence we have $|D_2| > 0$ if and only if $|D_3| > 0$ for the Routh - Hurwitz determinants $|D_2|$ and $|D_3|$ in this case.

We use the Set C in Table 3 as input parameters but change ϵ so that $\epsilon = 0$. In this case we find that $|D_1|(\eta^*) > 0$ in line with the theoretical considerations above. Hence, we have $|D_2|(\eta^*) > 0$. In fact, the numerical example displayed in Fig. 9 shows that $|D_1|$ is a strictly positive function of γ for all $\gamma \in [0, \eta^*]$. We have also been able to detect numerically two zeros, denoted by $h(1)$ and $h(2)$, of the function $|D_2|$ in the interval (η_m, η^*) for which $\frac{d}{d\gamma}|D_2|(h(1)) < 0 < \frac{d}{d\gamma}|D_2|(h(2))$ is satisfied, see Fig. 9. According to Shen and Jing (1995) and Nordbø et al. (2007), these zeros correspond to generic Hopf bifurcations in our modelling framework. By making use of the Routh–Hurwitz criterion, we conclude that the positive interior equilibrium point P_e ($\epsilon = 0$) given by (49) is asymptotically stable for $\gamma \in [\eta_m, h(1)) \cup (h(2), \eta^*)$. Notice that this stability result can be extended to the interval $(0, h(1)) \cup (h(2), \eta^*)$ by Theorem 2 in Appendix C (with $\epsilon = 0$). See the discussion above. In the regime $\gamma \in (h(1), h(2))$ the corresponding equilibrium point is unstable.

The frequency $\omega_{h(i)}$ (i=1,2) of the oscillations which are excited at the Hopf-point can be estimated by means of the formula

$$\omega^2_{h(i)} = \frac{a_3}{a_1} = \frac{qr\beta\zeta h(i)(1-\beta h(i))\Delta(h(i);\beta,\mu,\nu,\eta_0,p)}{q\nu\beta h(i)\Phi'(h(i);\eta_0,p)+1-\beta h(i)}, \quad i = 1,2. \tag{56}$$

Here a_1 and a_3 are coefficients of the characteristic polynomial (C8). We have made use of (C7)–(C11) (with $B = 0$) and (49) in the derivation of the frequency expression (56).

In Figs. 10 and 11 we demonstrate the excitation of the oscillations at the Hopf bifurcation points $\gamma = h(1)$ and $\gamma = h(2)$, for which the frequencies of these oscillations is approximately given by (56). We will not pursue any theoretical analysis of this problem, i.e., the derivation of the normal form associated with this bifurcation in order to determine the stability of the excited limit cycles. The numerical simulations also indicate that the oscillatory structure extends into the regime of finite ϵ. A notable feature here is that the amplitude of the oscillations increases when the harvesting rate parameter ϵ increases.

Then we consider the situation with $\epsilon = 0$. For $\gamma \in (h(1), h(2))$ we will get instability of the interior equilibrium point $P_e(\epsilon = 0)$. Moreover, for $0 < \gamma < \eta^*$, $\gamma \neq h(i)$ $(i = 1, 2)$, P_e $(\epsilon = 0)$ is a hyperbolic equilibrium point, from which it

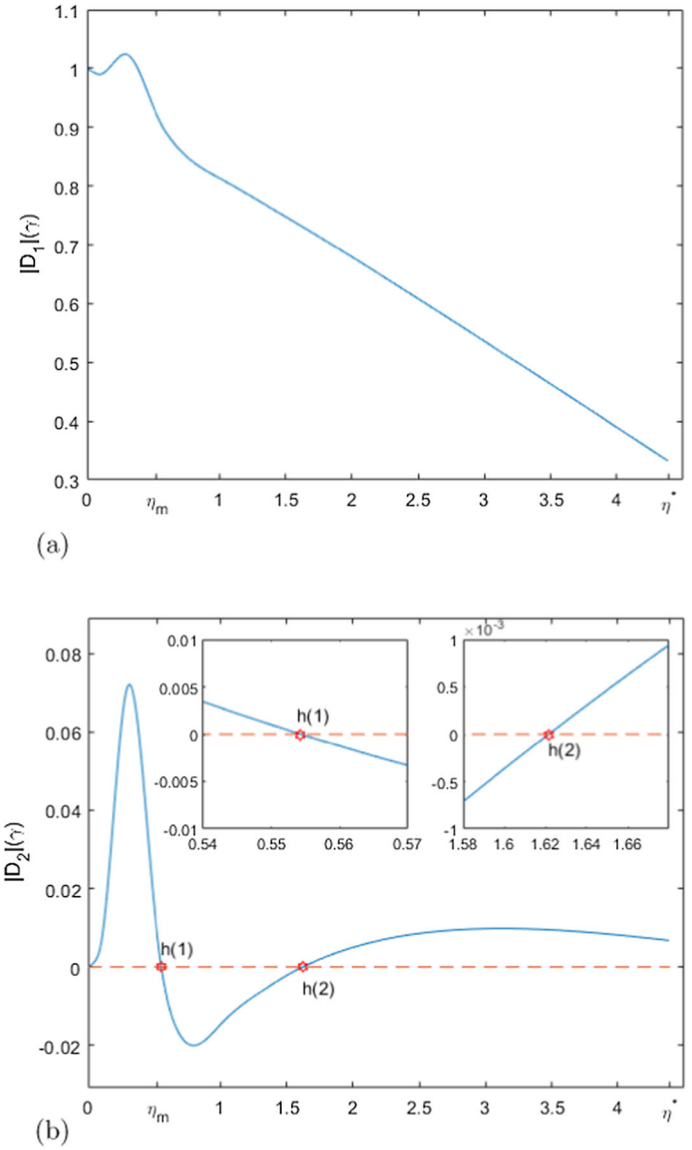

Fig. 9 The graphs of the Routh–Hurwitz determinants $|D_1|$ (**a**) and $|D_2|$ (**b**) as functions of the normalized mortality rate γ on the interval $[\eta_m, \eta^*]$. Here $\eta_m = 0.5264$ and $\eta^* = 4.393$. Input parameters: Set C in Table 3 except for ϵ and γ: $\epsilon = 0$ and γ is varied. The zeros $\gamma = h(1) = 0.5442$ and $\gamma = h(2) = 1.6216$ of $|D_2|$ are Hopf bifurcation points

follows that our dynamical system with $0 \leq \epsilon \ll 1$ is locally structurally stable in the vicinity of P_e in this parameter regime. Figure 12 confirms numerically the asymptotic stability of P_e when γ is in the interval $(0, h(1))$ or in the interval $(h(2), \eta^*)$, in accordance with Routh–Hurwitz criterion, see Appendix C. A notable feature which

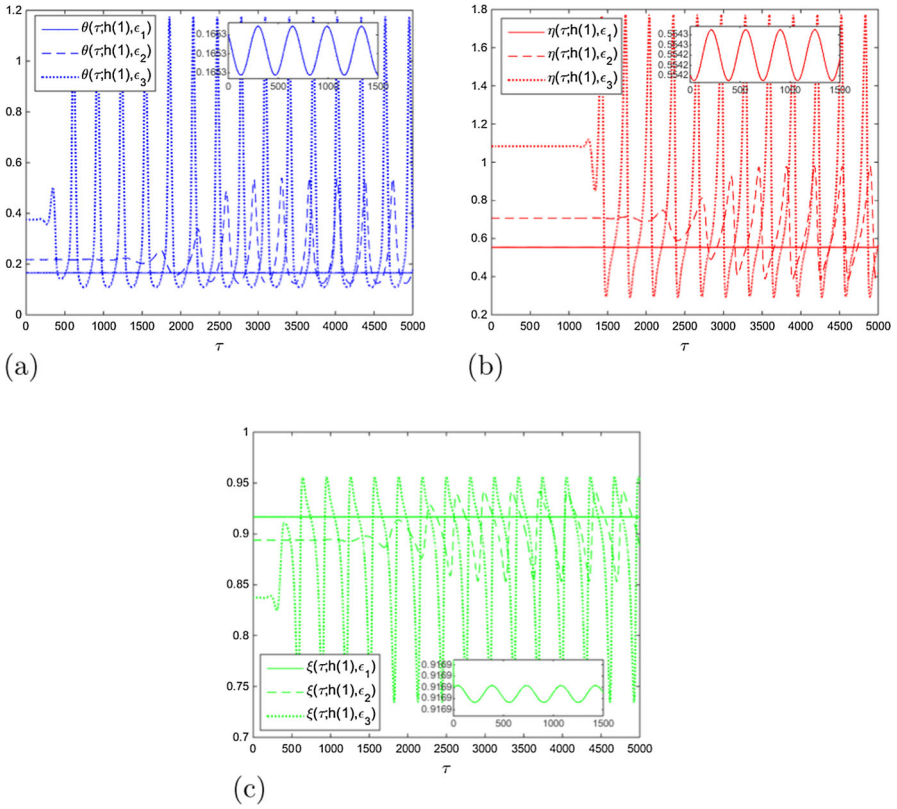

Fig. 10 Perturbations of the system (6)–(7) at the Hopf bifurcation point $\gamma = h(1) = 0.5442$, see Fig. 9. **a** The top predator density θ (blue), **b** the herbivore density η (red) and **c** the biomass density ξ (green) in the regimes: $\epsilon_1 = 0$ (solid lines), $\epsilon_2 = 0.05$ (dashed lines), $\epsilon_3 = 0.2$ (dotted lines). The insets show the oscillations generated at the Hopf bifurcation point $\gamma = h(1) = 0.5442$, $\epsilon_1 = 0$. Input data: Set C in Table 3 except for γ that is set equal to $h(1)$ and ϵ which is varied. The frequency $\omega_{h(1)}$ of the small amplitude oscillations for $\gamma = h(1)$, $\epsilon_1 = 0$ is computed by means of (56): $\omega_{h(1)} \approx 0.0053$ (Color figure online)

can be observed here is that the nonlinear stage of the instability detected for a $\gamma \in (h(1), h(2))$ evolves into a state consisting of stable oscillations. We expect that this oscillatory structure extends to the regime $0 < \epsilon \ll 1$, due to the local structural stability property in this parameter regime.

Finally, we would like to stress that the $2D$ herbivore—biomass model investigated in Bergland et al. (2019) does not allow for Hopf bifurcations, contrary to what we find for the present tritrophic model.

6 Saddle Node- and Hopf Bifurcations in the Case of Finite ϵ

We next study the variation and the number of interior equilibrium points as a function of ϵ (together with their respective stability characteristics) as well as saddle node bifurcations in our system. This means that we use ϵ as a control variable.

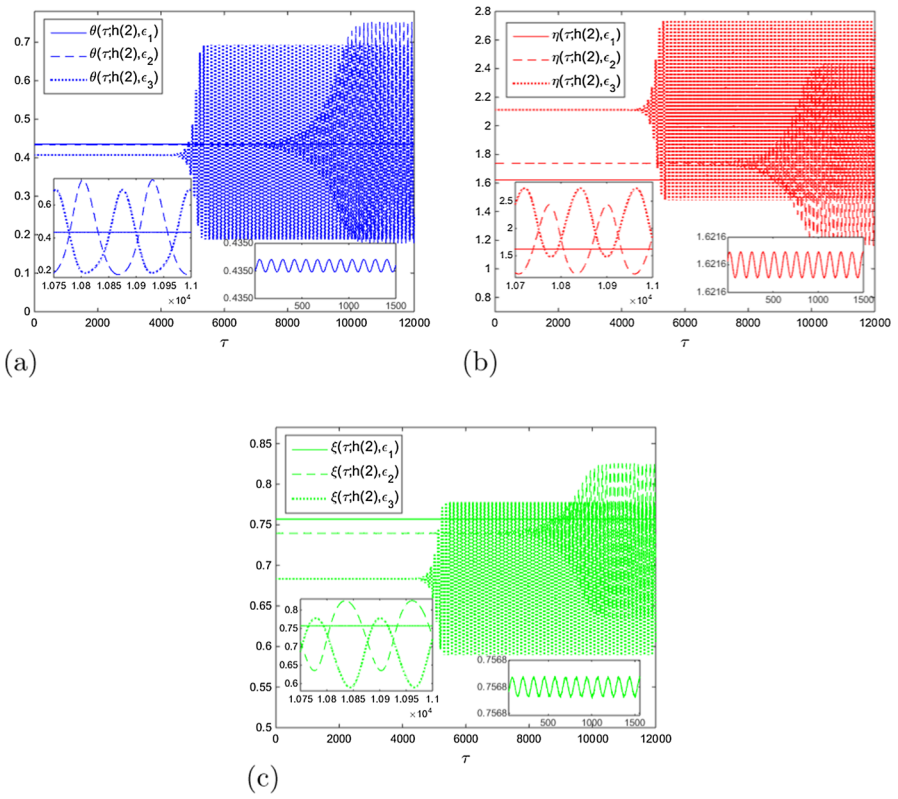

Fig. 11 Perturbations of the system (6)–(7) at the Hopf bifurcation point $\gamma = h(2) = 1.6216$, see Fig. 9. **a** The top predator density θ (blue), **b** the herbivore density η (red) and **c** the biomass density ξ (green) in the regimes: $\epsilon_1 = 0$ (solid lines), $\epsilon_2 = 0.05$ (dashed lines), $\epsilon_3 = 0.2$ (dotted lines). The insets show the oscillations generated at the Hopf bifurcation point $\gamma = h(2) = 1.6216$, $\epsilon_1 = 0$. Input data: Set C in Table 3 except for γ that is set equal to $h(2)$ and ϵ which is varied. The frequency $\omega_{h(2)}$ of the small amplitude oscillations for $\gamma = h(2)$, $\epsilon_1 = 0$ is computed by means of (56): $\omega_{h(2)} \approx 0.041$ (Color figure online)

In order to detect a saddle node bifurcation with ϵ as a control variable, we start out by noticing that the constant coefficient a_3 in the characteristic polynomial $\mathcal{P}_3$ defined by (C8) is equal to zero if and only if $W'(\eta_e; \epsilon) = 0$. Observing that $W(\eta_e; \epsilon) = 0$ for any interior equilibrium point $P_e = (\theta_e, \eta_e, \xi_e)$, we end up with the system of equations

$$\mathbf{G}(\eta_e, \epsilon) = \mathbf{0}, \quad \mathbf{G}(\eta_e, \epsilon) \equiv \begin{bmatrix} W(\eta_e; \epsilon) \\ W'(\eta_e; \epsilon) \end{bmatrix}, \tag{57}$$

for the bifurcation problem, see (33) and (34). We then observe that the mapping $\mathbf{G} : \mathbb{R}^2_+ \to \mathbb{R}^2$ is continuously differentiable. Assume that $(\eta_e, \epsilon) = (\eta_s, S)$ is solution to this problem where η_s belongs to the interior of $\mathcal{I}$, where $\mathcal{I}$ is defined by means of (32). We compute the Jacobian $D_{(\eta_e,\epsilon)}\mathbf{G}$ evaluated at this point and find that

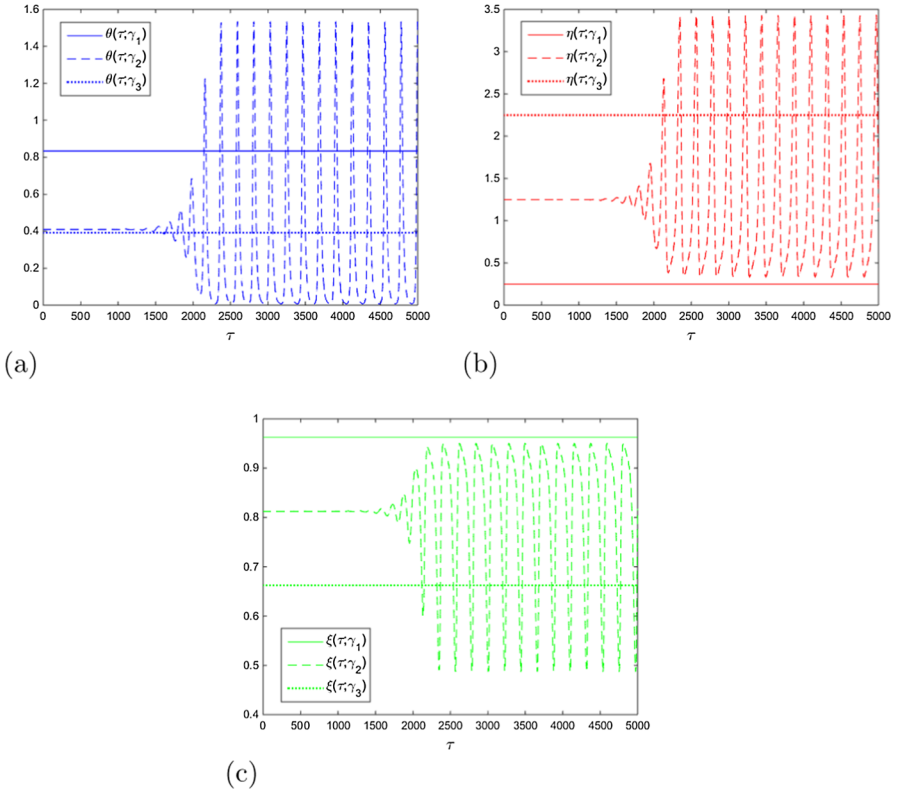

Fig. 12 The dynamical evolution in the vicinity of hyperbolic points of the system (6)–(7) for Set C except for ϵ which is set to 0 and γ which is varied as follows: $\gamma_1 = 0.25$ (solid lines), $\gamma_2 = 1.25$ (dashed lines), $\gamma_3 = 2.25$ (dotted lines). Notice that $\gamma_1 < h(1) < \gamma_2 < h(2) < \gamma_3$ where $h(1) = 0.5442$ and $h(2) = 1.6216$ (Hopf bifurcation values, see Figs. 9, 10 and 11) **a** The top predator density θ (blue), **b** the herbivore density η (red) and **c** the biomass density ξ (green) (Color figure online)

$$D_{(\eta_e,\epsilon)}\mathbf{G}(\eta_s, S) = \begin{bmatrix} W'(\eta_s; S) & \partial_\epsilon W(\eta_s; S) \\ W''(\eta_s; S) & \partial_\epsilon W'(\eta_s; S) \end{bmatrix} = \begin{bmatrix} 0 & \partial_\epsilon W(\eta_s; S) \\ W''(\eta_s; S) & \partial_\epsilon W'(\eta_s; S) \end{bmatrix}.$$

Here the symbol ∂_ϵ denotes partial derivative with respect to ϵ. Hence $D_{\eta_e,\epsilon}\mathbf{G}(\eta_s, S)$ is invertible if and only if

$$\det\left[D_{(\eta_e,\epsilon)}\mathbf{G}(\eta_s, S)\right] = -W''(\eta_s; S) \cdot \partial_\epsilon W(\eta_s; S) \neq 0. \tag{58}$$

The inverse function theorem now implies that there is an open set $\mathfrak{A}$ containing (η_s, S) and an open set $\mathfrak{B}$ containing $\mathbf{0}$ such that $\mathbf{G} : \mathfrak{A} \to \mathfrak{B}$ has a smooth inverse $\mathbf{H} : \mathfrak{B} \to \mathfrak{A}$ if the condition (58) is fulfilled. Therefore we conclude that (η_s, S) is not an accumulation points of zeros of $\mathbf{G}$, but an isolated zero provided (58) is satisfied. For ϵ close to S we generically get two solutions of the equation $W(\eta_e; \epsilon) = 0$ for which $W'(\eta_e; \epsilon) \neq 0$ signifying the existence of two equilibrium points that merge together at $\eta_e = \eta_s, \epsilon = S$.

Next, let us consider the equilibrium condition

$$\mathbf{F}(\mathbf{x}, \epsilon) = \mathbf{0}, \tag{59}$$

where the vector field $\mathbf{F}$ is defined as

$$\mathbf{F}(\mathbf{x}, \epsilon) \equiv \begin{bmatrix} r\zeta\theta\mathcal{H}(\mathbf{x}; \gamma, \epsilon, \theta_0, k) \\ q\beta\eta\mathcal{G}(\mathbf{x}; \varrho, \mu, \nu, \eta_0, p) \\ \xi\mathcal{F}(\mathbf{x}; \beta) \end{bmatrix},$$
$$\mathbf{x} = \begin{bmatrix} \theta_e \\ \eta_e \\ \xi_e \end{bmatrix}. \tag{60}$$

Here the component functions $\mathcal{H}$, $\mathcal{G}$ and $\mathcal{F}$ are defined by means of (7). Implicit differentiation with respect to ϵ now yields

$$D_{\mathbf{x}}\mathbf{F} \cdot \partial_\epsilon \mathbf{x} + D_\epsilon \mathbf{F} = \mathbf{0}. \tag{61}$$

Here $D_{\mathbf{x}}\mathbf{F}$ is the Jacobian of the vector field $\mathbf{F}$, whereas $D_\epsilon \mathbf{F}$ is the derivative with respect to ϵ of the same vector field. We readily find that the augmented Jacobian matrix $\left[D_{\mathbf{x}}\mathbf{F}\vdots D_\epsilon \mathbf{F}\right]$ evaluated at the bifurcation point $(\theta_s, \eta_s, \xi_s, S)$ has maximal rank, i.e.,

$$rank\left\{\left[D_{\mathbf{x}}\mathbf{F}\vdots D_\epsilon \mathbf{F}\right](\theta_s, \eta_s, \xi_s, S)\right\} = 3,$$

which is a characteristic feature of a saddle node bifurcation point, see Nayfeh and Balachandran (2008).

We finally study the variation of the equilibrium coordinates θ_e, η_e and ξ_e with ϵ. From (61) we get the component equations

$$\left.\begin{aligned} \partial_\epsilon \theta_e &= V'(\eta_e)[W'(\eta_e; \epsilon)]^{-1}\Phi(\theta_e; \theta_0, k), \\ \partial_\epsilon \eta_e &= [W'(\eta_e; \epsilon)]^{-1}\Phi(\theta_e; \theta_0, k), \\ \partial_\epsilon \xi_e &= -\beta[W'(\eta_e; \epsilon)]^{-1}\Phi(\theta_e; \theta_0, k). \end{aligned}\right\} \tag{62}$$

In the process of deriving these equations we have made use of (24) and (36). For the transversal crossing case $W'(\eta_e; \epsilon) \neq 0$, the rates $\partial_\epsilon \theta_e$, $\partial_\epsilon \eta_e$ and $\partial_\epsilon \xi_e$ are finite. Noticing that we have the non-transversality condition $W(\eta_s; S) = W'(\eta_s; S) = 0$ at saddle node bifurcation points $(\theta_s, \eta_s, \xi_s, S)$, we conclude by appealing to (62) that these rates become as expected infinite at this point. For $W'(\eta_s; S) < 0$, we observe that η_e decreases with ϵ. Hence, by making use of Theorem 1, we conclude that if η_e is a decreasing function of ϵ, then the corresponding equilibrium point P_e is unstable. Notice, however, a branch of an equilibrium point may remain unstable even though W' changes sign from negative to positive when passing a bifurcation point $(\eta_s; S)$. For asymptotically stable equilibrium points satisfying the bounding inequalities (32)

Table 6 Initial conditions used in the simulations of (6)–(7) leading to Figs. 15, 16, and 17

i	θ_i	η_i	ξ_i
1	0.432	0.35	0.96
2	0.23102	0.7324	0.89014
3	0.234548	0.739204	0.889119
4	0.2373	0.7446	0.8883
5	0.2676	3.0575	0.5414
6	0.257	3.1165	0.5325
H(1)	0.23487031	0.73982553	0.88902617
H(2)	0.26453806	3.0748432	0.53877352

(see Theorem 2), we find that $V'(\eta_e) < 0$ and $W'(\eta_e;\epsilon) > 0$ for $\eta_e \in [0, \eta_m]$ from which it follows that η_e increases with ϵ, whereas θ_e and ξ_e decrease with ϵ.

Figures 13 and 14 display the variation and the number of equilibrium points as a function of ϵ on the interval $0 \le \epsilon \le 0.43$ (Fig. 13a) and on the interval $0.72 \le \epsilon \le 0.98$ (Fig. 13b). These figures are constructed by using the MATCONT package in MATLAB. For the complementary interval $0.45 < \epsilon < 0.72$ there is a unique unstable equilibrium point for each ϵ, which we have chosen not to display graphically. The input parameter set for the computations leading to these figures is Set C in Table 3, except for ϵ which is varied. A notable feature in these two figures is the occurence of four saddle node bifurcation points for which one stable branch of equilibrium points merges together with an unstable branch of equilibrium points and then cease to exist when passing one of these values. The actual saddle node bifurcation values of ϵ are denoted by S_1, S_2, S_4 and S_5, For $\epsilon = S_3$ and $\epsilon = S_6$, we have the situation depicted in Figs. 13 and 14 where two unstable branches of equilibrium points merge together and cease to exist when passing one of these two values. Interestingly, we have detected two Hopf bifurcation points in the vicinity of S_3 and S_6 denoted by $H(1)$ and $H(2)$, respectively.

Remark 4 The Hopf bifurcation values $\epsilon = H(1)$ and $\epsilon = H(2)$ can be detected by exploiting the Routh–Hurwitz determinants in Appendix C with ϵ as a control variable, whereas the remaining parameters are as given in Set C in Table 3. The bifurcation values $\epsilon = H(1)$ and $\epsilon = H(2)$ satisfy the conditions $|D_1| > 0$, $a_3 > 0$, $|D_2| = 0$ and $\frac{d}{d\epsilon}|D_2| \neq 0$ for $\epsilon = H(1)$ and $\epsilon = H(2)$ by using the methodology presented in Shen and Jing (1995) and Nordbø et al. (2007). We do not pursue any details here.

In the remaining part of this subsection we will restrict ourselves to the ϵ-regime which produces bistability and the dynamical evolution as a function of ϵ in the vicinity of each of the two Hopf bifurcation points $\epsilon = H(1)$ and $\epsilon = H(2)$.

We observe the occurrence of a bistability for a narrow range of ϵ-values, i.e., $S_1 < \epsilon < S_2$. We clearly see the impact of the bistability on the dynamical evolution in Fig. 15, characterized by the division of the phase space into different attractor basins.

In Figs. 16 and 17 we display the dynamical evolution as a function of ϵ when ϵ is in the vicinity of the Hopf bifurcation points $\epsilon = H(1)$ and $\epsilon = H(2)$, respectively.

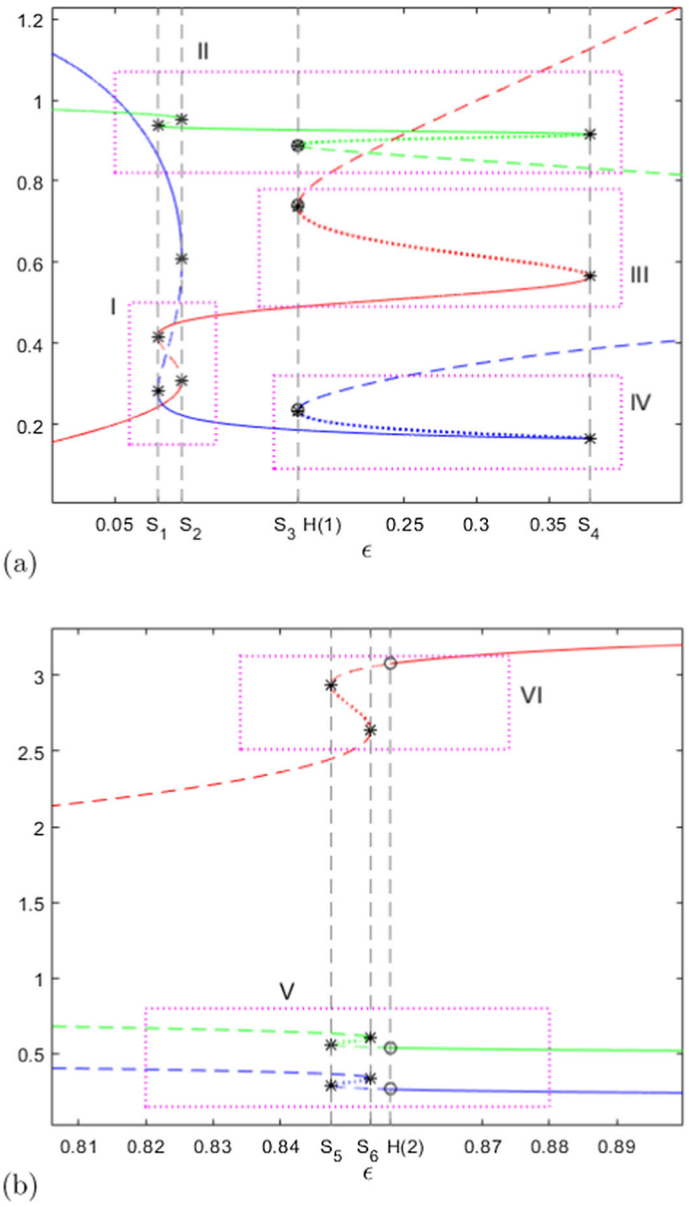

Fig. 13 Bifurcation diagram with ϵ as a control variable. **a** $0 \leq \epsilon \leq 0.45$. **b** $0.807 \leq \epsilon \leq 0.9$. Input data: Set C in Table 3 except for ϵ (or equivalently $\eta_{\max}$) which is varied. Blue curves (θ), red curves (η) and green curves (ξ); solid lines (stable branches), dashed and dotted lines (unstable branches). The saddle node points are marked with $*$, Hopf bifurcation points are marked with $\circ$. Zoomed versions of the rectangular regions I–VI are shown in Fig. 14 (Color figure online)

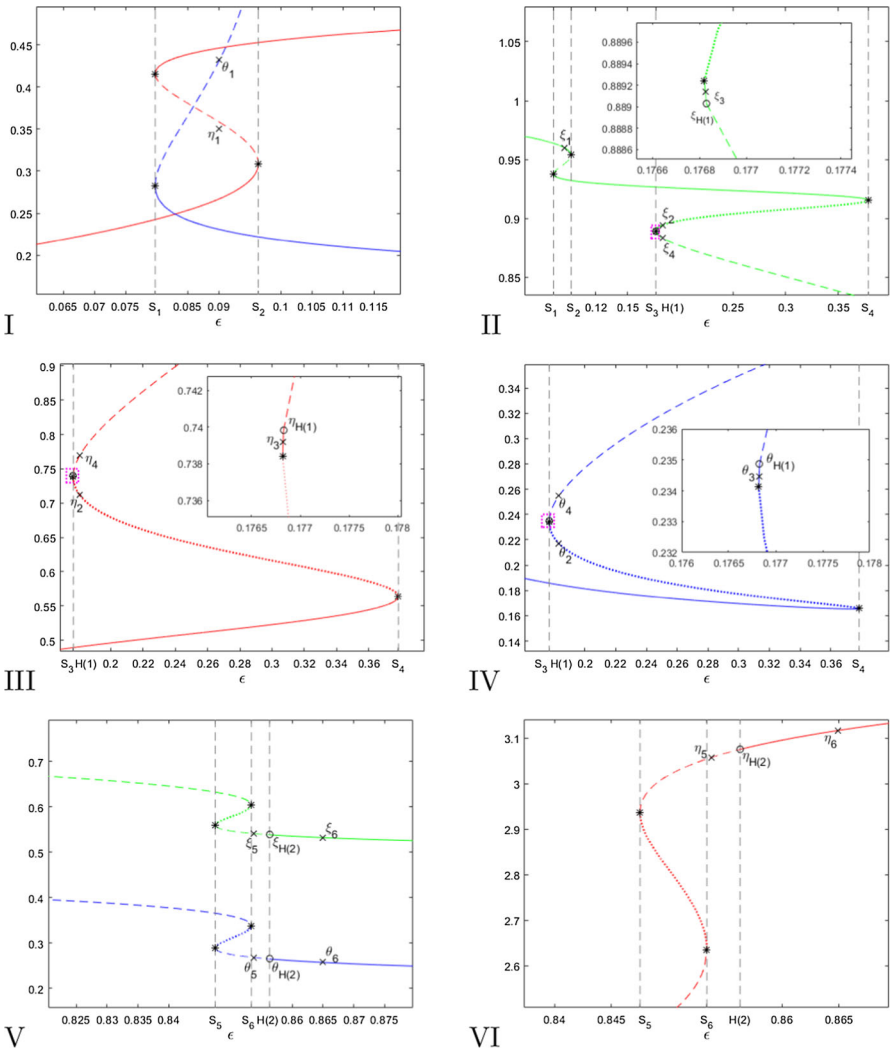

Fig. 14 Zoomed versions of the regions I–VI in Fig. 13. Blue curves (θ), red curves (η) and green curves ξ; solid lines (stable branches), dashed and dotted lines (unstable branches). The saddle node bifurcation values are given as $S_1 = 0.0796$, $S_2 = 0.0964$, $S_3 = 0.1769$, $S_4 = 0.3785$, $S_5 = 0.8470$ and $S_6 = 0.8535$. The Hopf bifurcation values are given as $H(1) = 0.17692968$ and $H(2) = 0.8563$. The saddle node- and the Hopf bifurcation points are marked with $*$ and $\circ$, respectively. The numerical values of the points $(\theta_i, \eta_i, \xi_i)$ (i=1,2,3,4,5,6) and the Hopf bifurcation points $(\theta_{H(i)}, \eta_{H(i)}, \xi_{H(i)})$ (i=1,2) are listed in Table 6 (Color figure online)

The results can be summarized as follows: For $\epsilon = H(1)$ and $\epsilon = H(2)$ with initial conditions chosen as the corresponding equilibrium points $(\theta_{H(1)}, \eta_{H(1)}, \xi_{H(1)})$ and $(\theta_{H(2)}, \eta_{H(2)}, \xi_{H(2)})$, respectively, we get in agreement with the Hopf bifurcation theory small amplitude oscillations.

In order to produce Fig. 16 we have selected three values of ϵ denoted by ϵ_2, ϵ_3 and ϵ_4, in addition to the Hopf-point $H(1)$, so that $\epsilon_2 < S_3 < H(1) < \epsilon_3 = \epsilon_4$. For $\epsilon = \epsilon_2$

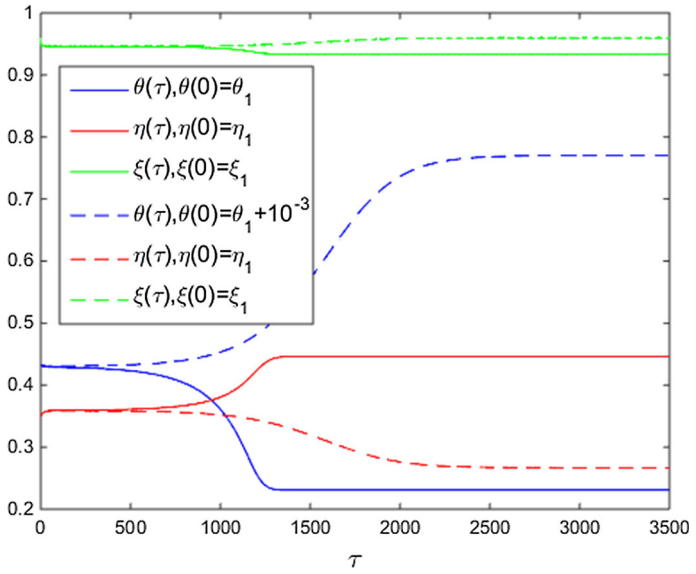

Fig. 15 The dynamical evolution and bistability. The parameter regime is $S_1 < \epsilon < S_2$ where $S_1 = 0.0796$ and $S_2 = 0.0964$ (bifurcation values, see Fig. 14). Input data: Set C in Table 3 except for ϵ which is chosen as $\epsilon = 0.085$. The initial condition $(\theta_1, \eta_1, \xi_1)$ coordinates are given in Table 6 and visualized in Fig. 14

we get a unique stable equilibrium point. In the corresponding numerical simulations we have chosen this equilibrium point as an initial condition. These simulations confirm the stability of this point. For the case $\epsilon = \epsilon_3 = \epsilon_4$ we have coexistence of three equilibrium states of which one is asymptotically stable and two are unstable. In the corresponding simulations we have selected two initial conditions in the vicinity of the unstable branches. The evolution in this case will settle down on the stable branch after the initial stage.

For Fig. 17 we extract the following conclusions: In addition to the Hopf bifurcation value $\epsilon = H(2)$ (which produces small amplitude oscillations), we select two ϵ-values denoted by ϵ_5 and ϵ_6 in the numerical runs. The ordering of these parameters are given as $S_6 < \epsilon_5 < H(2) < \epsilon_6$. For $\epsilon = \epsilon_6$, the stability of the corresponding unique equilibrium point is confirmed by choosing the equilibrium point as an initial condition. For $\epsilon = \epsilon_5$ we have unique equilibrium point which is a saddle point. After an initial phase the evolution settles down on stable relaxation type of oscillations. Each oscillation consists of a slow phase and a rapid phase. The slow phase consists of a motion on the associated stable manifold of the equilibrium point, whereas the rapid phase occurs as repelling behavior along the associated unstable manifold. The orbit rapidly twists back to the stable manifold and the outcome of this process is a closed orbit in the phase space. In Fig. 17d we have collected the integral curves produced for $\epsilon = \epsilon_5$ for the purpose of revealing more details regarding the interaction between the three population levels: In the rapid phase of each oscillation we first get an increase in the herbivore level until it reaches a maximum level and a dip in the biomass level. This is followed by an increase in the top predator level which also attains a maximum

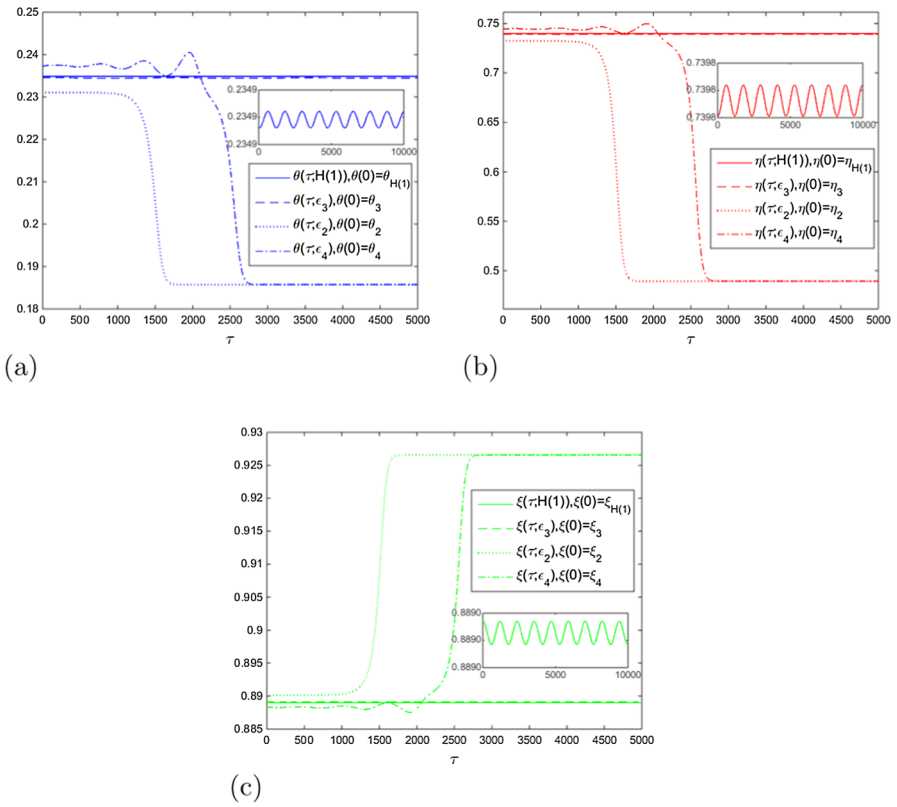

Fig. 16 The dynamical evolution of the system (6)–(7) for Sets C except for ϵ which is varied in the vicinity of S_3 and $H(1)$ (Hopf bifurcation value, see Fig. 14). Input data is Set C in Table 3 except for ϵ which is varied as follows in (**a**)–(**c**): $\epsilon = H_1$ (solid lines), $\epsilon = \epsilon_3 = 0.176822$ (dashed lines), $\epsilon = \epsilon_2 = \epsilon_4 = 0.177$ (dotted lines for the initial condition $(\theta_2, \eta_2, \xi_2)$ and dash-dotted line for the initial condition $(\theta_4, \eta_4, \xi_4)$). The ordering is $\epsilon_3 < S_3 < H(1) < \epsilon_2 = \epsilon_4$. The initial conditions are given in Table 6 and visualized in Fig. 14. The frequency $\omega_{H(1)}$ of the small amplitude oscillations for $\epsilon = H(1)$ is computed by means of the formula $\omega^2_{H(1)} = a_3/a_1$ where a_1 and a_3 are coefficients of the characteristic polynomial (C8): $\omega_{H(1)} \approx 0.0053$

level. The rapid increase in the top predator population level is followed by a rapid decline in the herbivore level which in turn leads to an increase in the biomass level and a rapid fall in the top predator level, before entering the slow phase of evolution.

7 The Dynamical Evolution as a Function of the Decimation Parameters: A Summary

We finally present an overview of the findings in Sects. 5 and 6. We express these results as a function of the decimation parameters ϵ and γ. We proceed as follows: For each fixed γ, we vary ϵ and construct the corresponding saddle node bifurcation diagram just in the same way as for $\gamma = 0.15$ (which is demonstrated in Figs. 13 and 14). We

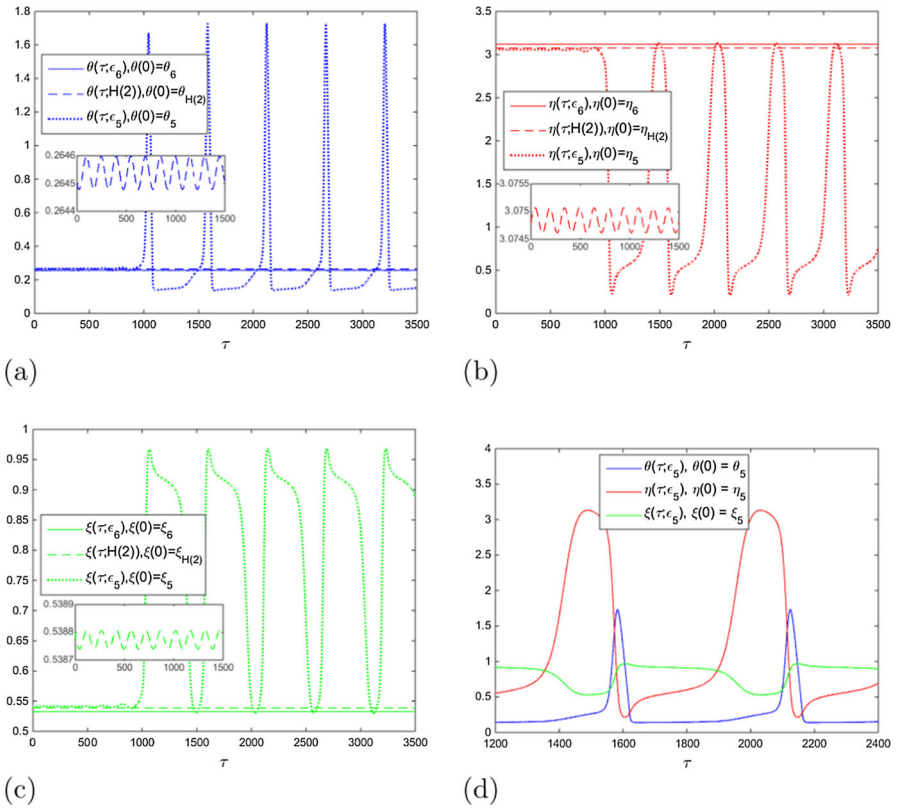

Fig. 17 The dynamical evolution of the system (6)–(7) for Set C except for ϵ which is varied in the vicinity of $H(2)$ (Hopf bifurcation value, see Fig. 14). Input data is Set C in Table 3 except for ϵ which is varied as follows in (**a**)–(**c**): $\epsilon_6 = 0.864948$ (solid lines), $\epsilon = H(2)$ (dashed lines), $\epsilon_5 = 0.85384$ (dotted lines). The ordering is $S_6 < \epsilon_5 < H(2) < \epsilon_6$. In (**d**) the interaction between the three population levels is demonstrated for $\epsilon = \epsilon_5$. The initial conditions coordinates are given in Table 6 and visualized in Fig. 14. The frequency $\omega_{H(2)}$ of the small amplitude oscillations for $\epsilon = H(2)$ is computed by means of the formula $\omega^2_{H(2)} = a_3/a_1$ where a_1 and a_3 are coefficients of the characteristic polynomial (C8): $\omega_{H(2)} \approx 0.041$

have also included the outcomes of the investigations resulting in Figs. 9,10,11,12 in this summary. The phase plot in Fig. 18 thus shows the correspondence between the γ, ϵ-plane and the final stage of the dynamical evolution of our modelling framework. The following features should be noted:

- For the red coloured, bounded region in the γ, ϵ-plane, the final stage consists of relaxation type of oscillations independently of the initial conditions which we select. This behavior is caused by the existence of a unique unstable interior equilibrium point of the saddle point type. Each oscillation consists of a slow phase and a rapid phase, as illustrated in Fig. 17d. The slow phase consists of a motion on the associated stable manifold of the equilibrium point, whereas the rapid phase occurs as repelling behavior along the associated unstable manifold. The orbit rapidly twists back to the stable manifold and the outcome of this process is a

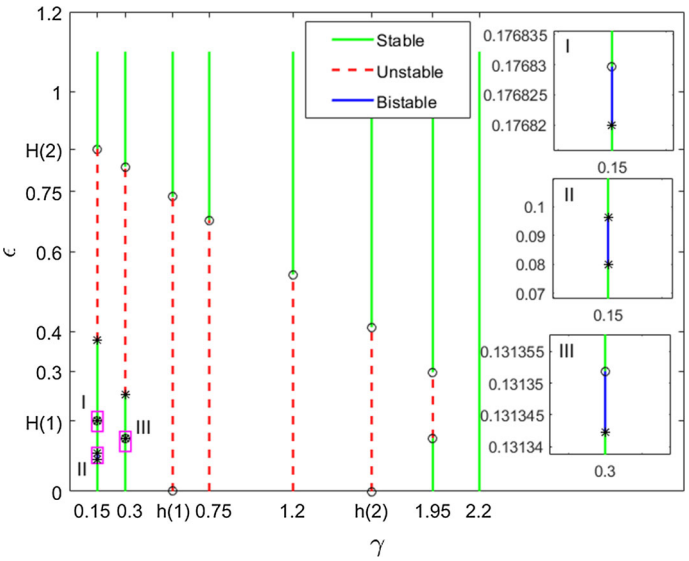

Fig. 18 The final stage of the dynamical evolution as a function of the top predator decimation parameters γ and ϵ. Points in the red coloured regions represent relaxation type of oscillations, whereas points in the green and blue coloured regions yield stabilization on equilibrium states. The saddle node- and the Hopf bifurcation points are marked with $*$ and $\circ$, respectively. Input data: Set C in Table 3, except for γ and ϵ (or equivalently $\eta_{\max}$) which are varied. $\gamma = h(1) = 0.5442$ and $\gamma = h(2) = 1.6216$ are the Hopf bifurcation values for $\epsilon = 0$ (see Fig. 9), whereas $\epsilon = H(1) = 0.17692968$ and $\epsilon = H(2) = 0.8563$ are the Hopf bifurcation values for $\gamma = 0.15$ (see Fig. 14) (Color figure online)

closed orbit in the phase space. For the complementary green coloured regions in this plane, the maximal number of equilibrium points is equal to three, of which at least one is an asymptotically stable equilibrium point. For this parameter regime, the integral curves end up on a stable state. Interestingly, the green coloured region in the γ, ϵ-plane appears as a union of two disjoint sets, which we will refer to as the lower- and the upper green region. The lower green region is the bounded region for which the origin in the γ, ϵ-plane belongs to its boundary. The points in this region are characterized by low natural mortality γ and low harvesting rate ϵ, whereas the upper region is the remaining green set. A comparison between the outcomes in the two regions goes as follows: The asymptotically stable states corresponding to points in the upper green region are typically characterized by a higher herbivore population level and lower biomass level as compared with the stable states originating from points in the lower region.

- We identify regimes which produce bistability (blue coloured region). In these regimes the dynamical evolution settles down on one of the asymptotically stable branches. In this case the stable branches divide the phase space into well separated attractor basins.
- The separatrix curves between the regions in the γ, ϵ-plane that definitely produce stable relaxation oscillations and asymptotically stable final states are determined by generic saddle node bifurcations for which one stable branch merge together

with an unstable branch. The branches of these equilibrium points cease to exist when passing the actual bifurcation values.

Remark 5 It will definitely be important if we can find observational data corresponding to the outcomes of saddle-node and Hopf-bifurcations which have been detected in the present model. As a starting point for this type of investigation we will point out that onset of temporal oscillations in the animal populations has been observed in Alaska (caribou–wolf interaction). See St John (2022). It is an open question whether Hopf–bifurcations in our model can serve as an explanatory framework for the driving mechanism behind these cycles. We do not pursue this problem here, however.

8 Concluding Remarks

8.1 Main Results

In this work we have investigated the dynamics of carnivore– herbivore–vegetation interactions, as a supplement to comparative static approaches, with particular emphasis on the dynamical evolution as a function of the natural morality and the harvesting rate of the carnivores. The model assumes the form of a Lotka–Volterra type of predator–prey model, where the carnivores and the herbivores play the role of predators and the vegetation biomass is the prey, and includes a density dependent harvesting rate and a linear mortality rate of the herbivores and the carnivores. This harvesting rate is modelled by means of sigmoidal functions in both the herbivore and the carnivore density. Moreover, the prey equation is an extended version of the logistic equation. The carrying capacity of the vegetation biomass and the conversion efficiency in the equations for the herbivores and the carnivores are assumed to be constant. Notice that the model under consideration simplifies to the herbivore—biomass system investigated in Bergland et al. (2019) when the top predator population is negligible. The modelling framework defines a globally wellposed system which satisfies the positive persistence property.

We have investigated the existence and stability of the equilibrium states of the modeling framework (6)–(7) as a function of the normalized mortality rate $\mu = m/qbK$, the normalized consumption rate $\beta = bk/\sigma$, the normalized saturated harvesting rate $\nu = H_0/qbK^2$ for the herbivores, the normalized mortality rate $\gamma = l/rcK$ of the top predators and the normalized saturated harvesting rate of the top predators $\epsilon = L_{\max}/rcK^2$.

Our findings can be summarized as follow:

In the regime of strong mortality, i.e., when $\mu > 1$ no positive equilibrium states exist. The dynamical evolution will in this case settle down on a state characterized by constant carrying capacity of the vegetation biomass and the extinction of both the herbivore and the top predator populations, i.e., the model permits the two boundary equilibrium points P_0 and P_1 of which P_0 is unstable, whereas P_1 is asymptotically stable. The transition case $\mu = 1$ corresponds to a non-hyperbolic equilibrium state for which the stability assessment based on the linearization procedure is not applicable.

For low and moderate degree of the herbivore mortality, i.e., when $0 \leq \mu < 1$ we have identified both existence and non-existence regimes of positive equilibrium states. One notable feature in this regime is thus the non-existence of such equilibrium points, contrary to what is found for the $2D$ herbivore—biomass model studied in Bergland et al. (2019). The existence issue of positive equilibrium states is resolved by means of the location of the interval $[\gamma, \eta_{\max}]$ relative the zeros of the function Δ. It turns out that the inequality $\gamma < \eta^*$ where η^* is the maximal zero of Δ is the necessary condition for existence of a positive equilibrium state. By noticing that $y^* \equiv K\eta^*$ plays the role of maximal herbivore equilibrium density in the aforementioned $2D$ herbivore—biomass model and by restoring to the dimensional variables, we find that y^* must exceed the threshold l/rcK in order to get positive equilibrium states of the tritrophic modelling framework (1). We also observe that the finite herbivore equilibrium density in this modelling framework will be reduced in comparison with the finite herbivore equilibrium density in the $2D$ model.

We have also explored the stability of the equilibrium states as a function of the normalized consumption rate β of the herbivores and illuminated the results with outcomes of numerical runs. The results of this investigation can be summarized as follows:

- In the high consumption rate regimes of the herbivores, i.e., when $\mathcal{Q}_m > 1$, $\beta > \beta_{cr}$ and $\mathcal{Q}_m \leq 1$, $\beta > \beta_{cr,2}$, we have a unique finite positive equilibrium which is asymptotically stable when $\gamma < \eta^*$. The boundary equilibrium states P_0, P_1 and P^* are all unstable in this regime. In the complementary regime $\gamma > \eta^*$ with no existence of positive interior equilibrium points, the boundary equilibrium states P_0 and P_1 remain unstable, whereas the boundary equilibrium point P^* is converted to an asymptotically stable equilibrium point.
- For the transition limit $\gamma \to \eta^*$, we will have that $P_e \to P^* = (0, \gamma, 1-\beta\gamma)$. This equilibrium state becomes a non-hyperbolic equilibrium for which the stability assessment based on linearization about the equilibrium state is not applicable.
- In the low and moderate consumption rate regimes of the herbivores i.e., when $\mathcal{Q}_m > 1$, $0 < \beta < \beta_{cr}$ and $\mathcal{Q}_m \leq 1$, $\beta_{cr,1} < \beta < \beta > \beta_{cr,2}$, we have coexistence of three boundary equilibrium points P_1^*, P_2^* and P_3^* together with the equilibrium states P_0 and P_1. The stability properties of P_1^*, P_2^* and P_3^* as a function of the mortality rate γ of the top-predators are summarized in Fig. 4, thus showing that P_2^* is always unstable saddle point, whereas P_1^* and P_3^* become asymptotically stable when γ exceeds η_1^* and η_3^*, respectively. We have identified parameter regimes for which there are no positive equilibrium states and necessary conditions for existence of such equilibrium states. The stability properties of the detected equilibrium points are investigated numerically together with numerical simulations which detail the temporal evolution of the state variables.
- The regime of low top predator harvesting regime ($0 < \epsilon \ll 1$). We have compared the outcome of the numerical simulations on this regime with the theoretical predictions deduced from regularly perturbed system. The number of positive interior equilibrium points collapses to one, whereas the number of boundary equilibrium points remains unaltered in this asymptotic limit.

- We have detected two generic Hopf bifurcations for positive interior equilibrium points numerically by means of the Routh Hurwitz determinants in the case of no harvesting of the top predators, i.e., when $\epsilon = 0$. We use the normalized mortality rate γ as a control variable and we operate in the parameter regime $0 \leq \mu < 1$, $\mathcal{Q}_m < 1$ and $0 < \beta < \beta_{cr,1}$. We apply the methodology outlined in Nordbø et al. (2007) where the existence of such bifurcations is related to the breakdown of the Routh–Hurwitz criterion. We have demonstrated the excitation of apparently stable oscillations in a whole window of γ-values in the vicinity of the Hopf bifurcation values of the this parameter. Interestingly, the excitation of these oscillations extends far beyond the theoretical predictions, thus supporting the conjecture that these oscillations are stable entities. The onset time of the oscillations, however, decreases with γ in this interval.
- We have constructed a saddle node diagram of the equilibrium states by means of the MATCONT package in MATLAB. Here we used the top predator harvesting rate parameter ϵ as a control variable. We have identified six saddle node bifurcation points and two Hopf bifurcation points for the chosen set of input parameters (i.e., Set C in Table 3). We have identified regimes for which we have coexistence of three equilibrium branches and their respective stability properties in some of the ϵ-regimes. We have found an interval of bistability which divides the phase space into a disjoint union of attractor basins for asymptotically stable states. In addition we have detected regimes for which we have a unique equilibrium state, which is either asymptotically stable or a saddle point. In case of a unique stable equilibrium state all integral curves approach this state, whereas in the unique saddle point case the final phase of any evolution consists of a relaxation type of robust and stable oscillations. The rapid phase within each period consists of an explosive growth in the herbivore population accompanied by a similar fast growth in the top predator population followed by subsequent rapid relaxation towards the slow phase. The biomass experiences a dip in the level during the rapid phase.

8.2 Possible Extensions

The present framework which is meant as a conceptualization, demonstrates possible evolutions and trade offs. In considering management policy, several complex elements and relevant topics should be included as extensions of the present modeling framework. Here we will list some possible extensions.

First of all, it will be of interest to extend the present modelling framework (1) with terms that describe depletion of the biomass. For the case of carnivore-rangifer-lichen model human harvesting of lichen biomass is less relevant. However, it seems like pasture deterioration may result from territorial conflicts, and that the animals' accessibility to the plant resources is subject to fluctuations. Such variations may be linked to more unstable weather conditions as a result of climate changes. Variations in temperature and precipitation affect the animals' ability to utilize grazing resources. Biomass degradation and accessibility is included in a 2D model analyzed in Bergland et al. (2019). We consider this as an important problem for future research.

In the present work we have omitted geographical distributions of range land, livestock and carnivores. An attempt to introduce more biological realism into this modeling framework is to include spatial effects, such as advection–diffusion effects, in a way analogous to Heilmann et al. (2018). Furthermore, we expect the carrying capacity K, the conversion efficiencies q and r as well as other parameters in our model to be subject to uncertainties, and one could model these parameters as stochastic processes, following the line of thought as for example in Evans (2012) and Øksendal (2003). In addition to human harvest, wildlife species populations are also threatened by habitat loss and other consequences of human activity, such as agriculture, mining, urban development, etc. (see Maxwell et al. 2016, Watson et al. 2019 and Horstkotte et al. 2022 for more details). Such phenomenon could be incorporated in the present modelling framework by assuming a temporal decay in the carrying capacity K, or by adding other temporal mechanism which causes biomass degradation and increasing animal mortality. We list these problems as a topic for future research.

Another reasonable extension could consist of including more detailed management policy discussions. Our analysis presumes that the harvesting rate is described as a given function of the animal populations. With this modelling assumption, we have seen that management policy is illustrated by means of variations in the parameters describing the harvesting rate functions. In future investigations the focus should also be on environmental and resource policies using a time discounting policy to handle the question of long-term benefits. Such policies could be based on maximizing the social welfare from a dynamic perspective, i.e., identifying preferred allocations of possible stable equilibrium states of the top predator population, the herbivore population and the biomass. Here several public regulatory mechanisms can play a role. This includes specific stock targets, harvest quotas, protected areas etc. and also indirect means such as taxes and subsidies, introduced in order to bring about a desirable development.

Appendix A: The Properties of the Function Δ: Boundary Equilibrium Points

For the sake of completeness we summarize here the properties of the function Δ defined by means of (14). This summary is based on Bergland et al. (2019).

For $\mu \geq 1$, $\Delta(\eta; \beta, \mu, \nu, \eta_0, p) < 0$ for all $0 \leq \eta_e \leq 1/\beta$. Let us consider the complementary regime $0 \leq \mu < 1$.

Since

$$\Delta(0; \beta, \mu, \nu, \eta_0, p) = 1 - \mu > 0,$$
$$\Delta(1/\beta; \beta, \mu, \nu, \eta_0, p) = -Q(1/\beta; \mu, \nu, \eta_0, p) < 0$$

in this case, the intermediate value theorem for continuous functions implies that there is at least one positive zero in the interval $(0, 1/\beta)$. The next step consists of determining the exact number of zeros of Δ as a function of the parameters β, μ, ν, η_0 and p. The analysis relies on the following observations:

- The function $\mathcal{Q}$ has a unique maximum point for $\eta \equiv \eta_m$. Moreover, $\mathcal{Q}(0; \mu, \nu, \eta_0, p) = \mu$ and $\lim_{\eta\to\infty} \mathcal{Q}(\eta; \mu, \nu, \eta_0, p) = \mu^{(+)}$. The maximum point $\eta_m = (p-1)^{1/p}\eta_0$ is determined by means of the condition $\mathcal{Q}'(\eta_m; \mu, \nu, \eta_0, p) = \Phi'(\eta_m; \eta_0, p) = 0$. The corresponding maximal value $\mathcal{Q}_m$ is given by (17).
- Non-transversal intersection points between the graphs of the functions $\mathcal{P}$ and $\mathcal{Q}$ are determined by the tangency condition

$$\Delta(\eta; \beta, \mu, \nu, \eta_0, p) = \Delta'(\eta; \beta, \mu, \nu, \eta_0, p) = 0 \tag{A1}$$

if they exist. Let $(\eta, \beta) = (\eta_{cr}, \beta_{cr})$ satisfy this system. We readily find that (η_{cr}, β_{cr}) that

$$\beta_{cr} = -\nu\Phi'(\eta_{cr}; \eta_0, p) \tag{A2}$$

from $\Delta' = 0$. By inserting this result into $\Delta = 0$ it is shown that $\eta = \eta_{cr}$ satisfies the equation

$$\Psi(\eta; \eta_0, p) = \frac{1-\mu}{\nu}, \quad \eta \in (\eta_m, \infty) \tag{A3}$$

where the function Ψ is a smooth function of η on the interval $[\eta_m, \infty)$ defined by

$$\Psi(\eta; \eta_0, p) \equiv \Phi(\eta; \eta_0, p) - \eta\Phi'(\eta; \eta_0, p). \tag{A4}$$

In Bergland et al. (2019) it is shown that the system (A2)–(A4) possesses at least one solution. Moreover, the maximal number of solutions is 2. This is the consequence of the following classification:

- *The regime* $\mathcal{Q}_m > 1$: In this case we find that the function Δ has a unique zero for $\beta > \beta_{cr}$ where β_{cr} satisfies the non-transversality condition (A1). In the complementary regime $0 \le \beta < \beta_{cr}$, we will get three equilibrium points. The tangency condition (A1) at $\eta = \eta_{cr}$ for $\beta = \beta_{cr}$ thus represents a transition state between the existence of single zero and the coexistence of three zeros.
- *The regime* $\mathcal{Q}_m < 1$: In this case the solution of the system (A1) consists of two points denoted by $(\eta_{cr,1}, \beta_{cr,1})$ and $(\eta_{cr,2}, \beta_{cr,2})$. The corresponding inclination parameters are called $\beta_{cr,1}$ and $\beta_{c,2}$, respectively, with $\beta_{cr,1} < \beta_{cr,2}$. We then get the following results: For the intervals $0 < \beta < \beta_{cr,1}$ and $\beta > \beta_{cr,2}$, the equation $\Delta = 0$ permits one and only one zero, whereas we have coexistence of three equilibrium points for the open interval $\beta_{cr,1} < \beta < \beta_{cr,2}$. The cases $\beta = \beta_{cr,1}$ and $\beta = \beta_{cr,2}$ represent transition states for which we get two zeros of the system (A1).
- *The transition state* $\mathcal{Q}_m = 1$: This transition state is equivalent with the non-transversality condition

$$\Delta(\eta_m; 0, \mu, \nu, \eta_0, p) = \Delta'(\eta_m; 0, \mu, \nu, \eta_0, p) = 0. \tag{A5}$$

This means that the graph of the function $\mathcal{P}$ is a parallel with the η-axis and tangent to the graph of the function $\mathcal{Q}$ at the point $(\eta_m, \mathcal{Q}_m)$. We notice that $(\eta_{cr,1}, \beta_{cr,1}) \to (\eta_m, 0)$ and $(\eta_{cr,2}, \beta_{cr,2}) \to (\eta_{cr}, \beta_{cr})$ continuously as $\mathcal{Q}_m \to 1^{(-)}$. Here (η_{cr}, β_{cr}) is the unique solution of $\Delta(\eta; \beta, \mu, \nu, \eta_0, p) = \Delta'(\eta; \beta, \mu, \nu, \eta_0, p) = 0$ for the case $\mathcal{Q}_m \to 1^{(+)}$.

In Fig. 19 we have depicted the graph of the function Δ in the regime $\mathcal{Q}_m > 1$ for different values of β in the vicinity of β_{cr}. Here we use the values of the herbivore parameters μ, ν, η_0 and p in Set A and Set B in Table 3 as input parameters. Figure 19 shows that the number of zeros of Δ changes from 1 to 3 when β is passing the critical value β_{cr}. In Fig. 20 we get a similar type of visualization in the regime $\mathcal{Q}_m < 1$ for β in the vicinity of the critical values $\beta_{cr,1}$ and $\beta_{cr,2}$, with a change in the number of zeros of Δ from 1 to 3 as we pass through $\beta_{cr,1}$ and $\beta_{cr,2}$ as characteristic feature. The plots in Figs. 19 and 20 are indeed consistent with the results summarized in Table 4.

Appendix B: Procedure for Determination of Positive Equilibrium Points

Here we outline the procedure for determination of the positive equilibrium points $P_e = (\theta_e, \eta_e, \xi_e)$. It is based on the results obtained in Sect. 3.3 and consists of the following steps:

1. Select the parameters $0 \le \mu < 1$, ν, p, η_0 and compute the maximum point η_m of the function $\mathcal{Q}$ and the corresponding maximal value $\mathcal{Q}_m$ defined by means of (17). According to Table 4, we have one non-transversal crossing point when $\mathcal{Q}_m > 1$ and two such points when $\mathcal{Q}_m \le 1$. Determine η_{cr} by solving the system (A3)–(A4). Then compute the critical value β_{cr} by means of the formula (A2).
2. Table 4 gives the number of positive equilibrium points of the biomass—herbivore model studied in Bergland et al. (2019) as function of β. These equilibrium states are the intersection points between the graphs of the function $\mathcal{P}(\eta_e; \beta) \equiv 1 - \beta\eta_e$ and $\mathcal{Q}(\eta_e; \mu, \nu, \eta_0, p) \equiv \mu + \nu\Phi(\eta_e; \eta_0, p)$. Determine the η_e-coordinates of these intersection points for one β-value in each of the β-intervals listed in Table 4. Identify the subintervals of the positive η_e-axis for which $\mathcal{P}(\eta_e; \beta) > \mathcal{Q}(\eta_e; \mu, \nu, \eta_0, p)$ (or equivalently $\Delta(\eta_e; \beta, \mu, \nu, \eta_0, p) \equiv \mathcal{P}(\eta_e; \beta) - \mathcal{Q}(\eta_e; \mu, \nu, \eta_0, p) > 0$, see definition (14)–(16). This means that we detect the set $\mathcal{D}_\Delta$ defined by means of (31).
3. Select the parameter γ such that γ is strictly less than the maximal zero of Δ. Then choose ϵ, θ_0 and k and compute $\eta_{\max}$ defined by means of (12) and (26).
4. Find the η_e-subinterval(s) of the interval $[\gamma, \eta_{\max}]$ for which $\Delta(\eta_e; \beta, \mu, \nu, \eta_0, p) > 0$. This means that we determine the subset $\mathcal{I}$ defined by means of (32). If positive equilibrium states exist, they will have η_e-coordinates in $\mathcal{I}$. These coordinates satisfy the system (33)–(34) on $\mathcal{I}$. By moving the interval $[\gamma, \eta_{\max}]$ along the η_e-axis, we can identify $\mathcal{I}$ in the different parameter regimes. Notice that we may for certain choices of γ and $\eta_{\max}$ find that $\mathcal{I} = \emptyset$ which means that we have no positive equilibrium points in spite of the fact that the biomass—herbivore model in Bergland et al. (2019) always possesses at least one positive equilibrium point when

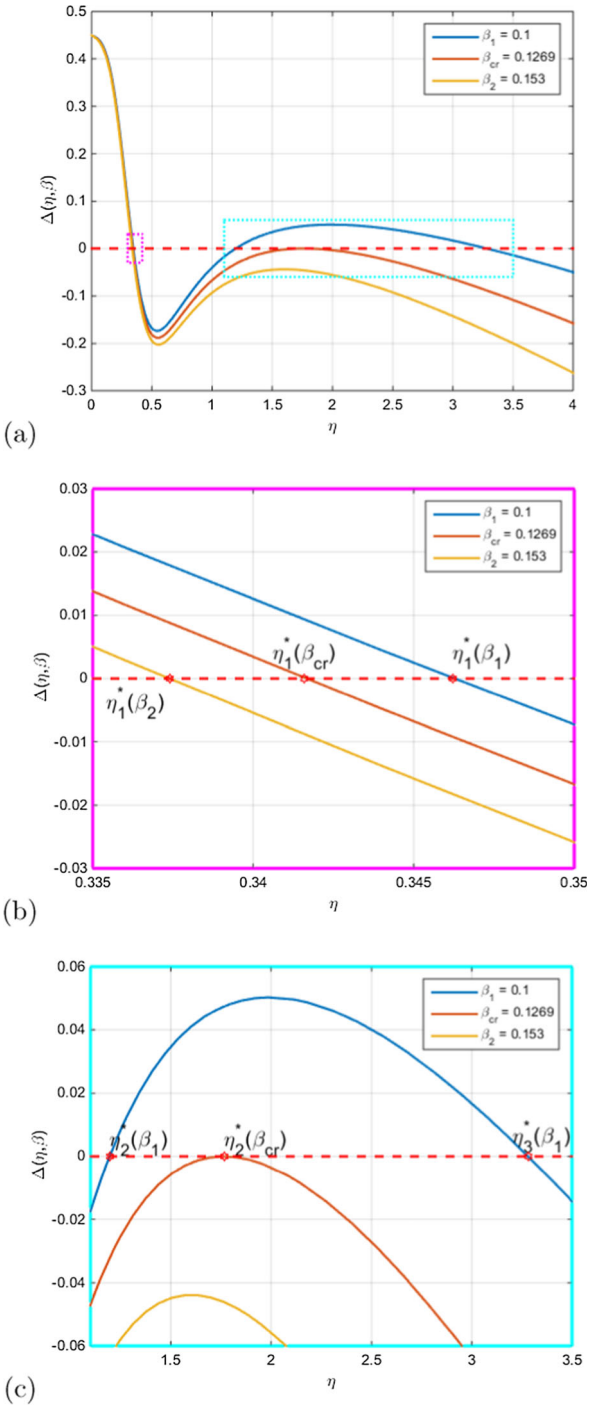

Fig. 19 **a** The graph of the function Δ as a function of η in the case $\mathcal{Q}_m > 1$ for different values of β. Here $\mathcal{Q}_m$ is defined by means of (17). **b** and **c** Magnified regions containing the zeros of the function Δ located in the purple and the turquoise rectangular domains in (**a**), respectively. The zeros of Δ are labeled by means of the corresponding β-value, whereas the subscript i is the counting index for the zero: $\eta_i^*(\beta)$. The input parameters are the herbivore parameters μ, ν, η_0 and p in Set A and Set B in Table 3. β_{cr} is computed by means of (A2)–(A4) in Appendix A Notice that the zeros of $\beta = 0.1$-curve in this plot produces the boundary equilibrium points P_1^*, P_2^* and P_3^* listed for Set A and Set B in Table 5

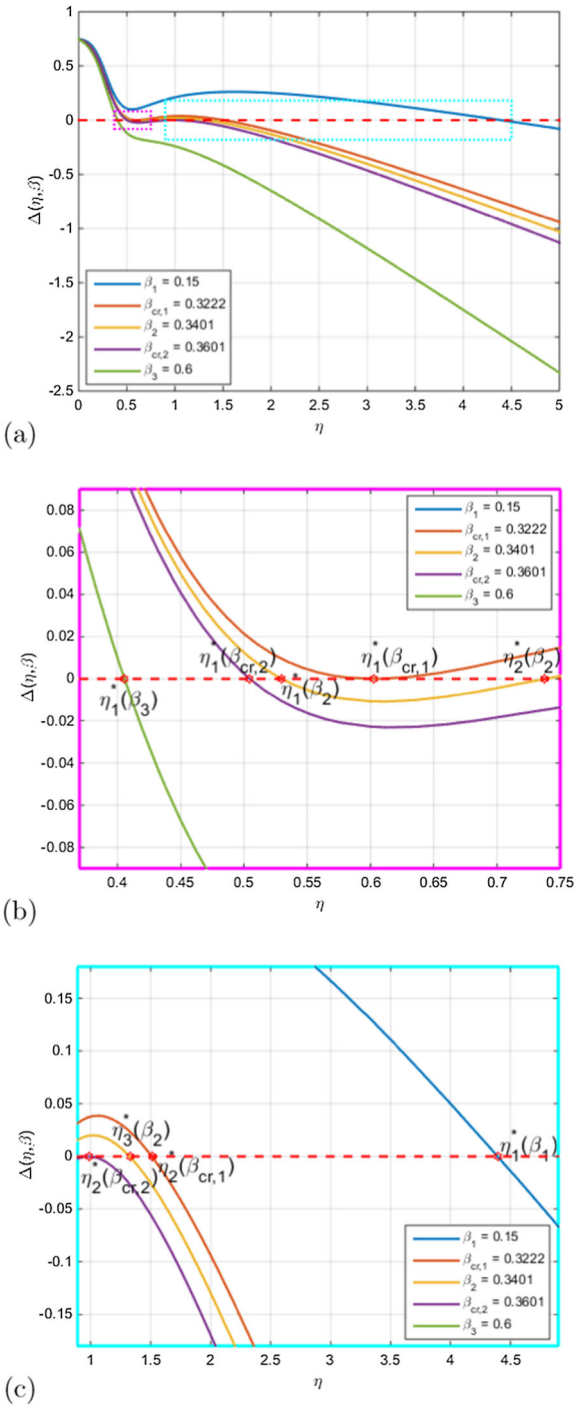

Fig. 20 **a** The graph of the function Δ as a function of η_e in the case $\mathcal{Q}_m \leq 1$ for different values of β. Here $\mathcal{Q}_m$ is defined by means of (17). **b** and **c** Magnified regions containing the zeros of the function Δ located in the purple and the turquoise rectangular domains in (**a**), respectively. The zeros of Δ are labeled by means of the corresponding β-value, whereas the subscript i is the counting index for the zero: $\eta_i^*(\beta)$. The input parameters are the herbivore parameters μ, ν, η_0 and p in Set C in Table 3. $\beta_{cr,1}$ and $\beta_{cr,2}$ are computed by means of (A2)–(A4) in Appendix A Notice that the zeros of $\beta = 0.15$-curve in this plot produces the boundary equilibrium point P_1^* listed for Set C in Table 5 (Color figure online)

$0 \leq \mu < 1$. We notice here that the information about top-predator parameters is stored in the decimation parameters γ and $\eta_{\max}$.

Appendix C: The Stability Assessment Methodology of the Positive Equilibrium Points Based on Routh–Hurwitz Determinants

For the positive interior equilibrium points $P_e = (\theta_e, \eta_e, \xi_e)$, the Jacobian is given as

$$D_{\mathbf{x}}\mathbf{F}(P_e) = \begin{bmatrix} r\zeta\theta_e\mathcal{H}_\theta(P_e) & r\zeta\theta_e\mathcal{H}_\eta(P_e) & 0 \\ q\beta\eta_e\mathcal{G}_\theta(P_e) & q\beta\eta_e\mathcal{G}_\eta(P_e) & q\beta\eta_e\mathcal{G}_\xi(P_e) \\ 0 & \xi_e\mathcal{F}_\eta(P_e) & \xi_e\mathcal{F}_\xi(P_e) \end{bmatrix} = \begin{bmatrix} -AB & A & 0 \\ -CD & -CE & C \\ 0 & -FG & -F \end{bmatrix} \tag{C6}$$

where the entries A, B, C, D, E, F and G are given as

$$\left.\begin{aligned} &A = r\zeta\theta_e, \quad B = \epsilon\Phi'(\theta_e; \theta_0, k), \quad C = q\beta\eta_e, \quad D = \varrho, \\ &E = \nu\Phi'(\eta_e; \eta_0, p), \quad F = \xi_e, \quad G = \beta. \end{aligned}\right\} \tag{C7}$$

The characteristic polynomial $\mathcal{P}_3$ corresponding to $D_{\mathbf{x}}\mathbf{F}(P_e)$ is the cubic polynomial

$$\mathcal{P}_3(\lambda) \equiv \det\left[\lambda\mathbf{I} - D_{\mathbf{x}}\mathbf{F}\right] = \lambda^3 + a_1\lambda^2 + a_2\lambda + a_3 \tag{C8}$$

where

$$\begin{aligned} a_1 &= AB + CE + F, \\ a_2 &= ABCE + ABF + ACD + CEF + CFG, \\ a_3 &= ACF(BG + BE + D). \end{aligned}$$

We get the following sufficient condition for instability:

Theorem 1 *Let $P_e = (\theta_e, \eta_e, \xi_e)$ denote a positive interior equilibrium point for which the function W defined by (34) satisfies the negative slope condition $W'(\eta_e) < 0$. Then P_e is unstable.*

Proof By making use of the expression (36) for W' and (C7), we readily find that the coefficient a_3 of the characteristic polynomial (C8) can be expressed as

$$a_3 = q\beta r\zeta\theta_e\eta_e\xi_e\varrho^{-1}W'(\eta_e).$$

Hence $a_3 < 0$ if and only if $W'(\eta_e) < 0$. We conclude that the characteristic polynomial $\mathcal{P}_3$ has at least one positive zero if $W'(\eta_e) < 0$, and the proof is completed. □

We now prove the following stability result:

Theorem 2 *Let $P_e = (\theta_e, \eta_e, \xi_e)$ denote a positive interior equilibrium point. If (θ_e, η_e) satisfies the bounding inequalities*

$$0 < \theta_e \leq (k-1)^{1/k}\theta_0, \quad 0 < \eta_e \leq (p-1)^{1/p}\eta_0, \tag{C9}$$

then P_e is asymptotically stable.

Proof The proof proceeds by using the Routh–Hurwitz criterion (Hurwitz et al. 1964). The Routh–Hurwitz determinants $|D_1|$, $|D_2|$ and $|D_3|$ of the characteristic polynomial (C8) are given as

$$|D_1| = a_1 = AB + CE + F, \tag{C10}$$

$$\left.\begin{aligned} |D_2| = a_1a_2 - a_3 = A^2B^2CE + A^2B^2F + A^2BCD \\ +ABC^2E^2 + 2ABCEF + ABF^2 \\ +AC^2DE + C^2E^2F + C^2EFG + CEF^2 + CF^2G, \end{aligned}\right\} \tag{C11}$$

$$|D_3| = a_3|D_2| = ACF(BG + BE + D)|D_2.| \tag{C12}$$

According to (C7), the parameters A, C, D, F and G are strictly positive. We notice that the parameters B and E are proportional to the derivatives $\Phi'(\theta_e; \theta_0, k)$ and $\Phi'(\eta_e; \eta_0, p)$, respectively, with positive proportionality constants. Hence $|D_i| > 0$ for $i = 1, 2, 3$ if the positive slope conditions $\Phi'(\theta_e; \theta_0, k) \geq 0$ and $\Phi'(\eta_e; \eta_0, p) \geq 0$ are satisfied. We notice that the coefficients $a_i, (i = 1, 2, 3)$ of the characteristic polynomial (C8) are strictly positive if $\Phi'(\theta_e; \theta_0, k) \geq 0$ and $\Phi'(\eta_e; \eta_0, p) \geq 0$. Hence, by appealing to the Routh - Hurwitz criterion, we conclude that all the zeros of $\mathcal{P}_3$ are located in the left λ-halfplane, i.e., $Re\{\lambda_i\} < 0$ for i=1,2,3 where $\mathcal{P}_3(\lambda_i) = 0$ if these positive slope conditions are fulfilled. This means that the positive equilibrium point P_e is asymptotically stable. Simple computation shows that $\Phi'(\theta_e; \theta_0, k) \geq 0 \Leftrightarrow 0 < \theta_e \leq (k-1)^{1/k}\theta_0$ and $\Phi'(\eta_e; \eta_0, p) \geq 0 \Leftrightarrow 0 < \eta_e \leq (p-1)^{1/p}\theta_0$. This completes the proof. □

Appendix D: Global Wellposedness of the Modelling Framework

Here we prove the following result:

Theorem 3 *The initial value problem of the system (1) [or equivalently (6)–(7)] is globally wellposed in the first orthant of the phase space.*

Proof We start out by expressing the system (6) on the compact vector form

$$\frac{d\mathbf{x}}{d\tau} = \mathbf{F}(\mathbf{x}) \tag{D13}$$

with the right-hand side defined by (37).

We then notice that the right-hand side $\mathbf{F}$ (which is a continuously differentiable vector field with respect to $\mathbf{x}$) can be viewed as an operator on the space of continuous functions that satisfies the following so-called locally Lipschitz condition: For any $r > 0$, there exists a strictly positive constant $L(r)$ such that for any $\mathbf{x}, \mathbf{y} \in \mathbb{R}^3$, $|\mathbf{x}| \leq r$, $|\mathbf{y}| \leq r$, it holds true that

$$|\mathbf{F}(\mathbf{x}) - \mathbf{F}(\mathbf{y})| \leq L(r)|\mathbf{x} - \mathbf{y}|. \tag{D14}$$

Here we have made use of the distance $|\mathbf{a} - \mathbf{b}| = \max_{i=1,2,3} |a_i - b_i|$ in the space $\mathbb{R}^3$ (here $\mathbf{z} = (z_1, z_2, z_3)^T$).

The Lipschitz constant $L(r)$ is given as

$$L(r) = \mathfrak{a}r + \mathfrak{b}$$

where

$$\mathfrak{a} = \max\{2r\zeta, 2q\beta(1+\varrho), 2(1+\beta)\},$$

$$\mathfrak{b} = \max\left\{ r\zeta\left(\gamma + \epsilon\frac{p\eta_0^p\left(\frac{\eta_0^p(p-1)}{p+1}\right)^{\frac{p-1}{p}}}{\left(\frac{\eta_0^p(p-1)}{p+1} + \eta_0^p\right)^2}\right), q\beta\left(\mu + \nu\frac{k\theta_0^k\left(\frac{\theta_0^k(k-1)}{k+1}\right)^{\frac{k-1}{k}}}{\left(\frac{\theta_0^k(k-1)}{k+1} + \theta_0^k\right)^2}\right), 1\right\}.$$

Let us equip (6) with an arbitrary initial condition $\mathbf{x}(0) = \mathbf{x}_0$ located in the first orthant of $\mathbb{R}^3$. The initial value problem obtained is equivalent to the fixed-point problem

$$\mathbf{x}(\tau) = (\mathfrak{F}\mathbf{x})(\tau), \tag{D15}$$

where the operator $\mathfrak{F}$ is defined as

$$(\mathfrak{F}\mathbf{x})(\tau) \equiv \mathbf{x}_0 + \int_0^\tau \mathbf{F}(\mathbf{x}(s))ds.$$

Let us now construct a solution to (D15), which is also a solution to the initial value problem for (6).

We first take $r_1 = 2|\mathbf{x}_0|$ and find $T_1 = \frac{1}{2(\mathfrak{a}r_1 + \mathfrak{b})}$. Then the operator $\mathfrak{F}$ is a contraction in the space of continuous functions defined on the segment $[0, T_1]$ with the norms that do not exceed r_1 (the constant of contraction is $1/2$). Applying Banachs fixed-point theorem, we prove unique solvability of (D15) with the initial condition $\mathbf{x}(0) = \mathbf{x}_0$ on $[0, T_1]$. Moreover, the maximal deviation of the solution obtained, denoted by $\mathbf{x}_{T_1}$, is less or equal to r_1, i.e., its norm on the space of continuous functions defined on the segment $[0, T_1]$ is less or equal to r_1.

The next step consists of using $\mathbf{x}_{T_1}(T_1)$ as the new initial condition. Assume that $r_2 = 2r_1$ and solve the system (D15) on the time interval $[T_1, T_1 + T_2]$ where $T_2 =$

$\frac{1}{2(ar_2+b)}$ by applying Banachs fixed-point theorem. Thus we have extended $\mathbf{x}_{T_1}$ to the interval $[0, T_1 + T_2]$, obtaining a unique solution, say $\mathbf{x}_{T_2}$, of the initial value problem on $[0, T_1+T_2]$. We also notice that the norm of $\mathbf{x}_{T_2}$ in the space of continuous functions defined on $[0, T_1 + T_2]$ is less than $r_2 = 2r_1$.

In the next step, we take the new initial condition as $\mathbf{x}_{T_2}(T_1 + T_2)$. Assuming the boundedness of the norms by letting $r_3 = r_2 + r_1$, we find a unique extension of $\mathbf{x}_{T_2}$ to the interval $[0, T_1 + T_2 + T_3]$ where $T_3 = \frac{1}{2(ar_3+b)} = \frac{1}{2(3ar_1+b)}$, which solves the initial value problem on $[0, T_1 + T_2 + T_3]$. We thus extend the τ-interval for existence and uniqueness of solution to (D15) and, hence, to the initial value problem for (D13). Noticing that on the n-th step of the procedure described above, the extension of the domain of the solution has the length $\frac{1}{2(ar_1 n+b)}$, we conclude that the solution we construct does not develop a singularity in finite time. This means that it can be extended to the whole interval $[0, \infty)$. Thus we have constructed a unique solution $\mathbf{x}_\infty = (\theta, \eta, \xi)^T$, where the component functions θ, η and ξ are continuous functions, which due to the form of the right hand side of (6), implies that smoothness of the solution with respect to τ is obtained. □

Acknowledgements The authors will like to thank B.Sc. Trym Asvald Bergland, B.Sc. Vitaly Yarema, Cand.Agric Asbjørn Olafsen and M.Sc. Ørjan Fosdahl Kristensen for their assistance in the preparation phase of the present paper. We are also grateful to Professor Ola Flåten (The Arctic University of Norway), Professor Arcady Ponosov, Dr. Purnendu Mishra, Professor Øystein Holand (Norwegian University of Life Sciences), Dr Barkha Tiwari (Norwegian Institute for Water Research), Professor Mads Peter Sørensen, Dr. Adam Mielke, Professor Jens Juul Rasmussen (Technical University of Denmark) and Professor Evgeny Zhukovskiy (Derzhavin Tambov State University, Russia) for fruitful and stimulating discussions during the preparation phase of this paper. Most of the the present work was completed in December 2022 when J. Wyller was a Guest Researcher at Department of Applied Mathematics and Computer Science, Technical University of Denmark. J. Wyller will like to express his sincere gratitude to Technical University of Denmark for kind hospitality during the stay. J. Wyller gratefully acknowledges the financial support from internal funding scheme at Norwegian University of Life Sciences (Project Number 1211130114), which financed the international stay at Department of Applied Mathematics and Computer Science, Technical University of Denmark, Denmark. The authors would also like to thank the reviewers for constructive remarks.

Funding The research is supported by the academic leadership program Priority 2030. The work of E. Burlakov was supported by RFBR and FRLC, Project Number 20-511-23001.

Data availability Data sharing not applicable to this article as no datasets were generated or analysed during the current study.

Declarations

Conflict of interest The authors have no competing interests to declare that are relevant to the content of this article.

References

Åhman B, Rasmus S, Risvoll C et al (2022) Large predators and their impact on reindeer husbandry. In: Reindeer Husbandry and Global Environmental Change. Routledge, pp 118–130

Andrén H, Linnell JD, Liberg O et al (2006) Survival rates and causes of mortality in Eurasian lynx (lynx lynx) in multi-use landscapes. Biol Cons 131(1):23–32

Arnold VI (1988) Geometrical methods in the theory of ordinary differential equations. Springer, New York

Barman B, Ghosh B (2019) Explicit impacts of harvesting in delayed predator–prey models. Chaos Solitons Fract 122:213–228
Bautista C, Revilla E, Naves J et al (2019) Large carnivore damage in Europe: analysis of compensation and prevention programs. Biol Conserv 235:308–316
Beddington J, May R (1980) Maximum sustainable yields in systems subject to harvesting at more than one trophic level. Math Biosci 51(3):261–281
Bergland H, Wyller J, Burlakov E (2019) Pasture–Livestock dynamics with density-dependent harvest and changing environment. Nat Resour Model 32(4):e12,213
Boitani L, Linnell JD (2015) Bringing large mammals back: large carnivores in Europe. Rewilding Eur Landscapes. Springer, Cham, pp 67–84
Brekke KA, Øksendal B, Stenseth NC (2007) The effect of climate variations on the dynamics of pasture–livestock interactions under cooperative and noncooperative management. Proc Natl Acad Sci 104(37):14730–14734
Brown G, Berger B, Ikiara M (2005) A predator–prey model with an application to lake victoria fisheries. Mar Resour Econ, pp 221–248
Chapron G, Kaczensky P, Linnell JD et al (2014) Recovery of large carnivores in Europe's modern human-dominated landscapes. Science 346(6216):1517–1519
Clark C (2010) Mathematical bioeconomics. The Mathematics of Conservation, Wiley, New York
de Roos AM (2014) Modeling population dynamics. University of Amsterdam, The Netherlands
Evans LC (2012) An introduction to stochastic differential equations, vol 82. American Mathematical Society, Berkeley
Flaaten O (1988) The economics of multispecies harvesting: theory and application to the Barents Sea fisheries. Studies in Contemporary Economics. Springer, Berlin
Flaaten O (1991) Bioeconomics of sustainable harvest of competing species. J Environ Econ Manag 20(2):163–180
Ghosh B, Kar T (2013) Possible ecosystem impacts of applying maximum sustainable yield policy in food chain models. J Theor Biol 329:6–14
Ghosh B, Kar T, Legovic T (2014a) Relationship between exploitation, oscillation, msy and extinction. Math Biosci 256:1–9
Ghosh B, Kar TK, Legović T (2014b) Sustainability of exploited ecologically interdependent species. Popul Ecol 56(3):527–537
Guckenheimer J, Holmes P (1983) Nonlinear oscillations, dynamical systems, and bifurcations of vector fields. Springer, New York
Heilmann IT, Thygesen UH, Sørensen MP (2018) Spatio-temporal pattern formation in predator-prey systems with fitness taxis. Ecol Complex 34:44–57
Hogarth W, Norbury J, Cunning I et al (1992) Stability of a predator–prey model with harvesting. Ecol Model 62(1):83–106
Horstkotte T, Kumpula J, Sandström P et al (2022) Pastures under pressure: effects of other land users and the environment. In: Reindeer husbandry and global environmental change. Routledge, pp 76–98
Huang J, Gong Y, Ruan S (2013) Bifurcation analysis in a predator–prey model with constant-yield predator harvesting. Discrete Contin Dyn Syst Ser B 18:2101–2121
Hurwitz A et al (1964) On the conditions under which an equation has only roots with negative real parts. Sel Pap Math Trends Control Theory 65:273–284
Johannesen AB (2014) Sámi reindeer herding (samisk reindrift). In: Flåten, Skonhoft (eds) The economics of natural resources (Naturressursenes Økonomi). Gyldendal Akademisk, Oslo, Norway (In Norwegian)
Johannesen AB, Skonhoft A (2009) Local common property exploitation with rewards. Land Econ 85(4):637–654
Johannesen AB, Olaussen JO, Skonhoft A (2019) Livestock and carnivores: economic and ecological interactions. Environ Resour Econ 74(1):295–317
Kaczensky P, Chapron G, Von Arx M et al (2013) Status, management and distribution of large carnivores-bear, lynx, wolf & wolverine-in Europe. Tech. rep., (Report to the EU Commission, Part 1 and Part 2, 2013) http://ec.europa.eu/environment/nature/conservation/species/carnivores/pdf/task1part1statusofineurope.pdf and http://ec.europa.eu/environment/nature/conservation/species/carnivores/pdf/task1part2speciescountryreports.pdf
Kojola I, Tuomivaara J, Heikkinen S et al (2009) European wild forest reindeer and wolves: endangered prey and predators. In: Annales Zoologici Fennici, BioOne, pp 416–422

Legović T, Klanjšček J, Geček S (2010) Maximum sustainable yield and species extinction in ecosystems. Ecol Model 221(12):1569–1574
Li B, Liu S, Cui J et al (2016) A simple predator–prey population model with rich dynamics. Appl Sci 6(5):151
Logan JD (1987) Applied mathematics: a contemporary approach. Wiley, New York
Mattisson J, Odden J, Nilsen EB et al (2011) Factors affecting Eurasian lynx kill rates on semi-domestic reindeer in northern Scandinavia: can ecological research contribute to the development of a fair compensation system? Biol Cons 144(12):3009–3017
Maxwell SL, Fuller RA, Brooks TM et al (2016) Biodiversity: the ravages of guns, nets and bulldozers. Nature 536(7615):143–145
May RM, Beddington JR, Clark CW et al (1979) Management of multispecies fisheries. Science 205(4403):267–277
Murray J (2002) Mathematical biology, I: an introduction, Vol. 17 of Interdisciplinary Applied Mathematics. Springer, New York
Nayfeh AH, Balachandran B (2008) Applied nonlinear dynamics: analytical, computational and experimental methods. Wiley, Weinheim
NEA (2022) Environmental status. Tech. rep., The Norwegian Environment Agency, http://www.miljodirektoratet.no/globalassets/publikasjoner/dirnat2/attachment/405/gaupe-jerv-bjorn-ulv-og-kongeorn.pdf, in Norwegian
Nordbø Ø, Wyller J, Einevoll GT (2007) Neural network firing-rate models on integral form. Biol Cybern 97(3):195–209
Øksendal B (2003) Stochastic differential equations. Springer, Berlin
Paul P, Kar T, Ghorai A (2016) Ecotourism and fishing in a common ground of two interacting species. Ecol Model 328:1–13
Persson J, Ericsson G, Segerström P (2009) Human caused mortality in the endangered Scandinavian wolverine population. Biol Conserv 142(2):325–331
Ripple WJ, Estes JA, Beschta RL et al (2014) Status and ecological effects of the world's largest carnivores. Science 343(6167)
Sæther BE, Engen S, Persson J et al (2005) Management strategies for the wolverine in Scandinavia. J Wildl Manag 69(3):1001–1014
Shen J, Jing Z (1995) A new detecting method for conditions of existence of hopf bifurcation. Acta Math Appl Sin 11(1):79–93
Skonhoft A, Johannesen AB, Olaussen JO (2017) On the tragedy of the commons: When predation and livestock loss may improve the economic lot of herders. Ambio, pp 1–11
St John JR (2022) Understanding Caribou Population Cycles. University of Montana, undergraduate thesis
Tromeur E, Loeuille N (2017) Balancing yield with resilience and conservation objectives in harvested predator–prey communities. Oikos 126(12):1780–1789
Tveraa T, Stien A, Brøseth H et al (2014) The role of predation and food limitation on claims for compensation, reindeer demography and population dynamics. J Appl Ecol 51(5):1264–1272
Van Eeden LM, Crowther MS, Dickman CR et al (2018) Managing conflict between large carnivores and livestock. Conserv Biol 32(1):26–34
Vasil'eva AB, Butuzov VF, Kalachev LV (1995) The boundary function method for singular perturbation problems, vol 14. SIAM, Philadelphia
Vázquez FJ, Watt R (2011) Copyright piracy as prey–predator behavior. J Bioecon 13(1):31–43
Watson R, Baste I, Larigauderie A et al (2019) Summary for policymakers of the global assessment report on biodiversity and ecosystem services of the intergovernmental science-policy platform on biodiversity and ecosystem services. IPBES Secretariat, Bonn